



Ramblings on superconducting magnet cooling for accelerators

(based on CAS-course Austria-2023)

TE-MSC seminar – CERN 15-02-2024

R. van Weelderen (CERN)

With contributions from P. Borges de Sousa (CERN), T. Kottig (CERN), F. Ferrand (CERN)

Outline

- Introduction
 1. Intent
 2. Main cooling-option drivers
- Temperature levels
 1. Introduction
 2. Cryogenic fluids
- Helium as a cold-source
 1. Phase diagram
 2. Intermezzo Hell - conduction through superfluid helium (Hell)
 3. Conduction comparative
- Intermezzo: Magnet-examples
- Temperature levels
 1. “Why do we need to talk about it”
 2. “That’s why we need to talk about it”
- Fully immersed in Hell:
- LHC dipoles and HL-LHC cable-stacks
- Bayonet HX cooling scheme
- Numerical tool & application to HL-LHC Nb₃Sn quadrupoles
- Helium availability and typical LHC reliance (fully immersed magnets)
- Food for thought of operating fully helium immersed accelerator magnets
- Some points to remember
- References

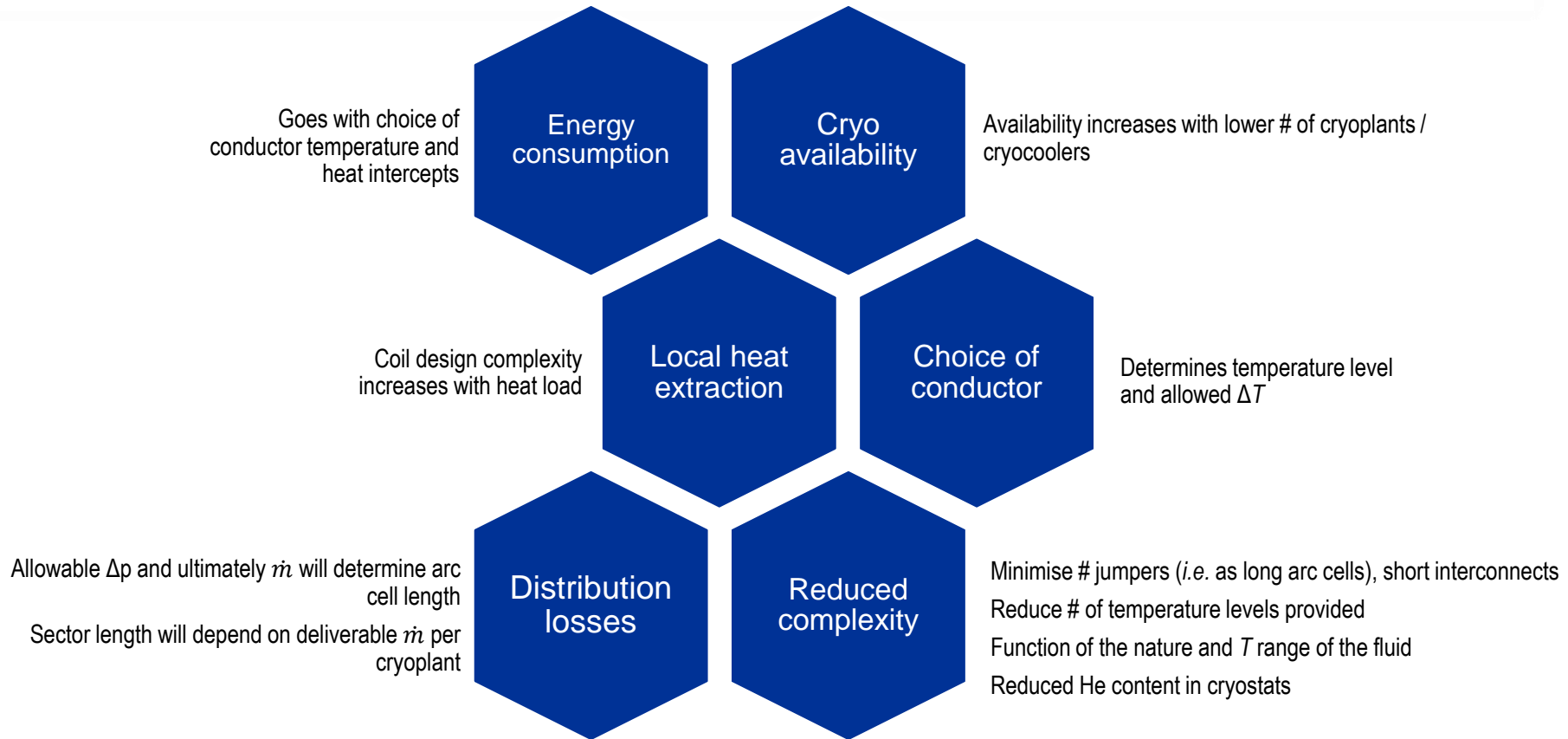
Introduction: Intent

The intent is to introduce *aspects of cryogenics* that enter the reflection of choosing a development direction when tasked with a superconducting magnet design.

We'll *familiarize* you with the major elements involved that arise in a coherent/optimized design *satisfying the magnet performance requirements on the one hand and on the other hand the cryogenic drivers of sustainability* (i.e. minimizing operational cost, infrastructure, complexity), safety constraints,...

The talk reflects my personal opinion

Introduction: main cooling-option drivers



All “drivers” are interlinked, even if not shown adjacent

We'll mainly focus on Energy consumption & Local heat extraction

Temperature levels: introduction

Superconducting magnets come in *many variants and applications* ranging from small medical devices, motors, wind-power generators, huge particle detectors and plasma containing structures to km-long particle accelerators,...

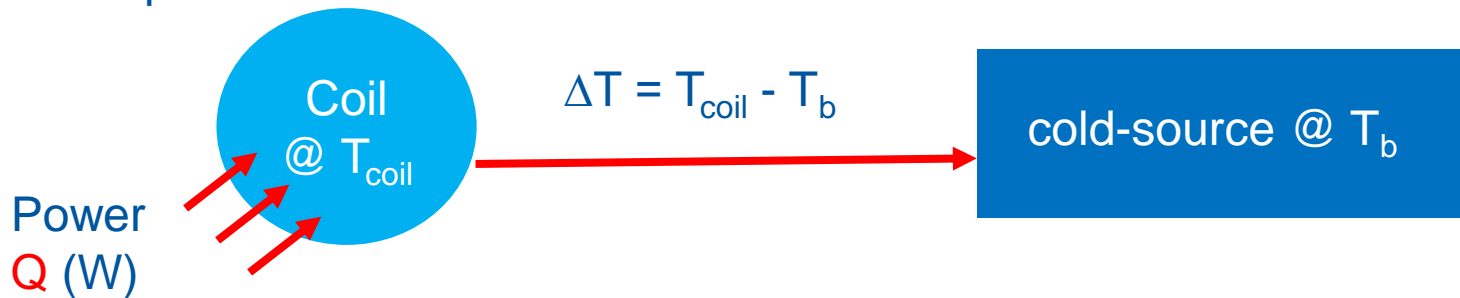
The most common superconductors, NbTi, Nb₃Sn, MgB₂, HTS making up the magnet coils *generally operate at temperatures from 1.9 K – 4.5 K – 20 K < 77 K*

Temperature levels: Cryogenic fluids

THERMOPHYSICAL PROPERTIES

The choice of cryogenic fluid in the cooling system is principally driven by:

1. T_b : boiling temperature at atmospheric pressure of 1.013 bar
 - The boiling temperature provides a fixed “*base reference temperature*” for the cooling system. It will be the lowest temperature available. All cooled devices, will function at *slightly higher temperatures* depending on implementation specifics.



The ΔT originates from an accumulation of: conduction through solid material, solid-fluid interface resistances, conduction through cooling fluids, pressure drops in the cooling fluid system

Temperature levels: Cryogenic fluids

THERMOPHYSICAL PROPERTIES

The choice of cryogenic fluid in the cooling system, is principally driven by *(not counting distribution losses)*:

2. The latent heat “ L_h ” of evaporation at T_b (kJ/kg)
 - The latent heat determines the rate of liquid to evaporate per power at cold

21 W for 1 g/s of helium @ 4.2 K
199 W for 1 g/s of nitrogen @ 77 K

$$\frac{dm}{dt} = \frac{Q}{L_h}$$

Temperature levels: Cryogenic fluids

THERMOPHYSICAL PROPERTIES

Fluid	⁴ He	N ₂	Ar	H ₂	O ₂	Kr	Ne	Xe	Air	Water
Boiling temperature 1.013 bar (K)	4.2	77.3	87.3	20.3	90.2	119.8	27.1	165.1	78.8	373
Latent heat (evaporation at Tb) kJ/kg	21	199.1	163.2	448	213.1	107.7	87.2	95.6	205.2	2260
Ratio volume gas (273 K) /liquid	709	652	795	798	808	653	1356	527	685	-----
Specific mass of liquid (at Tb) – kg/m ³	125	804	1400	71	1140	2413	1204	2942	874	960

Given the present use of superconductors for accelerators (NbTi, Nb₃Sn) **helium** is applied as main cooling fluid, with sometimes **nitrogen** for thermal shields.
*Future HTS use might open-up the use of **liquid hydrogen** (but has many issues to be solved).*

Temperature levels: Cryogenic fluids

Comparison:

1L LHe: $\approx 12 - 50$ € and *rising/fluctuating*

1L LN₂: ≈ 0.1 €

Quantity to cooldown 1 kg of stainless steel

Using	Latent heat only	Latent heat and enthalpy of gas
LHe from 290 to 4.2 K	29.5 litre	0.75 liter
LHe from 77 to 4.2 K	1.46 litre	0.12 litre
LN2 from 290 to 77 K	0.45 litre	0.29 litre

Helium as a cold-source: phase-diagram

Helium behaves as any "normal-fluid" in the domain indicated by Hel ("normal helium")

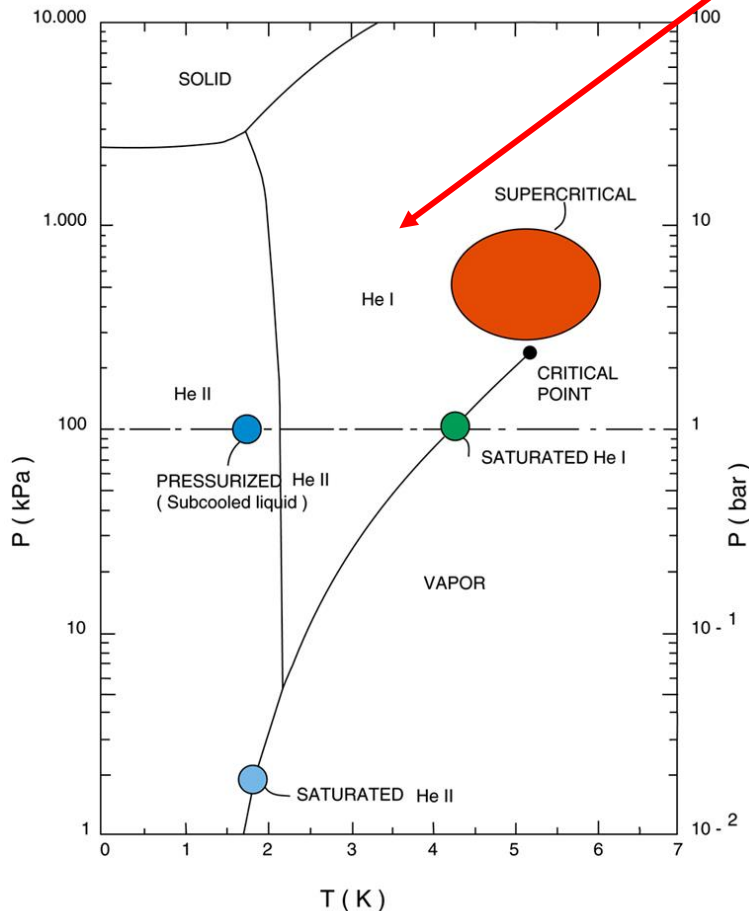
Helium behaves as a "super-fluid" in the domain indicated by HeII ("superfluid helium")

Working domain of saturated helium II is along the saturation line from (starting from 5.0 kPa & 2.17 K, to typically 1.6 kPa & 1.8 K)

Working domain of pressurised helium II, by subcooling liquid at any pressure above saturation, typically near atmospheric pressure (100 kPa).

Additional advantage of functioning in pressurized superfluid helium is that subatmospheric pressures are avoided, thus minimizing the impact of air-inleaks, and the good electrically isolating properties (compared with low pressure helium).

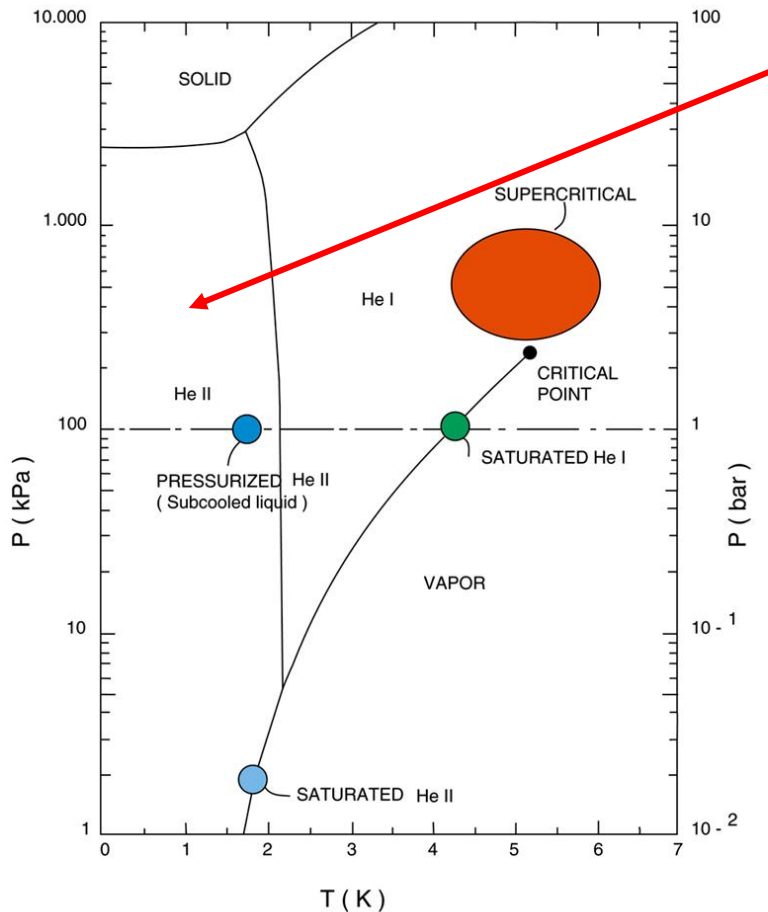
Phase diagram of helium



CERN AC - CR106 - 13/03/96

Helium as a cold-source: phase-diagram

Phase diagram of helium



CERN AC - CR106 - 13/03/96

Helium behaves as any "normal-fluid" in the domain indicated by HeI ("normal helium")

Helium behaves as a "super-fluid" in the domain indicated by HeII ("superfluid helium")

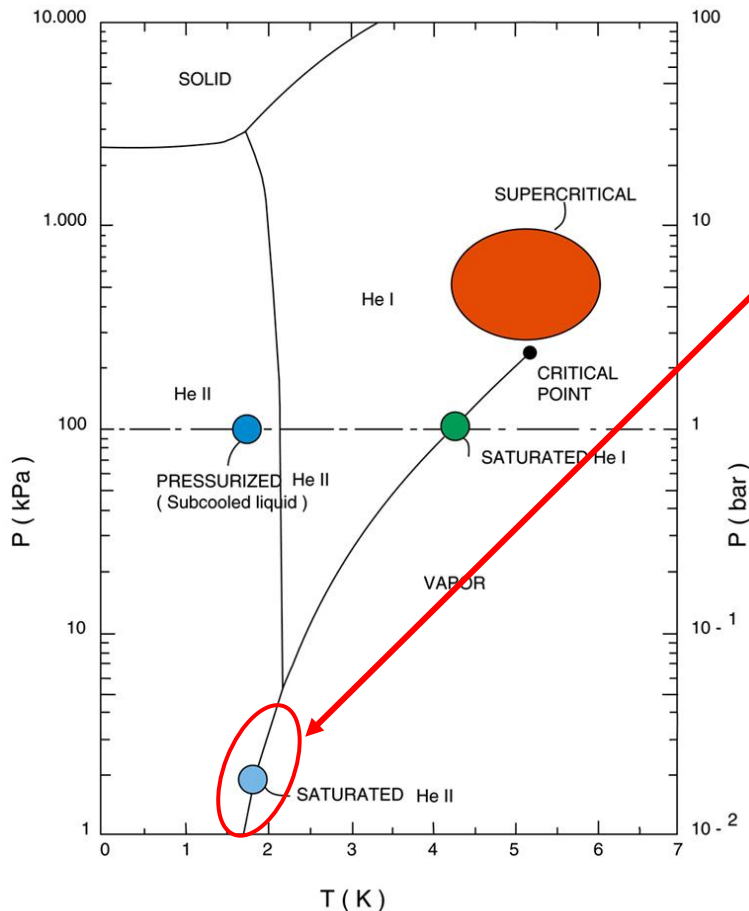
Working domain of saturated helium II is along the saturation line from (starting from 5.0 kPa & 2.17 K, to typically 1.6 kPa & 1.8 K)

Working domain of pressurised helium II, by subcooling liquid at any pressure above saturation, typically near atmospheric pressure (100 kPa).

Additional advantage of functioning in pressurized superfluid helium is that subatmospheric pressures are avoided, thus minimizing the impact of air-inleaks, and the good electrically isolating properties (compared with low pressure helium).

Helium as a cold-source: phase-diagram

Phase diagram of helium



CERN AC - CR106 - 13/03/96

Helium behaves as any "normal-fluid" in the domain indicated by HeI ("normal helium")

Helium behaves as a "super-fluid" in the domain indicated by HeII ("superfluid helium")

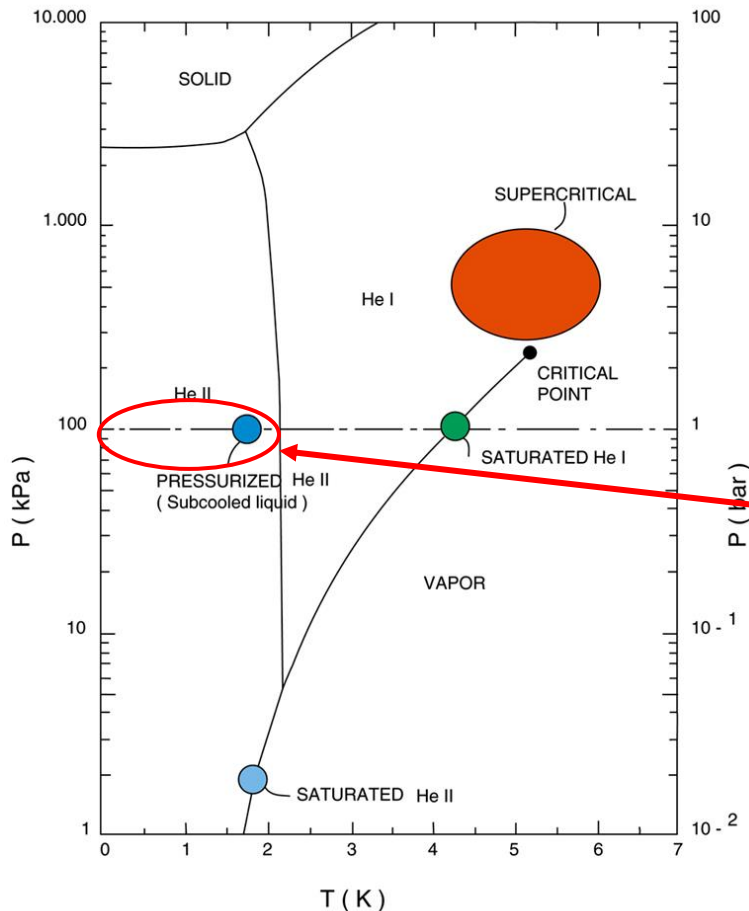
Working domain of saturated helium II is along the saturation line from (starting from 5.0 kPa & 2.17 K, to typically 1.6 kPa & 1.8 K)

Working domain of pressurized helium II, by subcooling liquid at any pressure above saturation, typically near atmospheric pressure (100 kPa).

Additional advantage of functioning in pressurized superfluid helium is that subatmospheric pressures are avoided, thus minimizing the impact of air-inleaks, and the good electrically isolating properties (compared with low pressure helium).

Helium as a cold-source: phase-diagram

Phase diagram of helium



CERN AC - CR106 - 13/03/96

Helium behaves as any "normal-fluid" in the domain indicated by HeI ("normal helium")

Helium behaves as a "super-fluid" in the domain indicated by HeII ("superfluid helium")

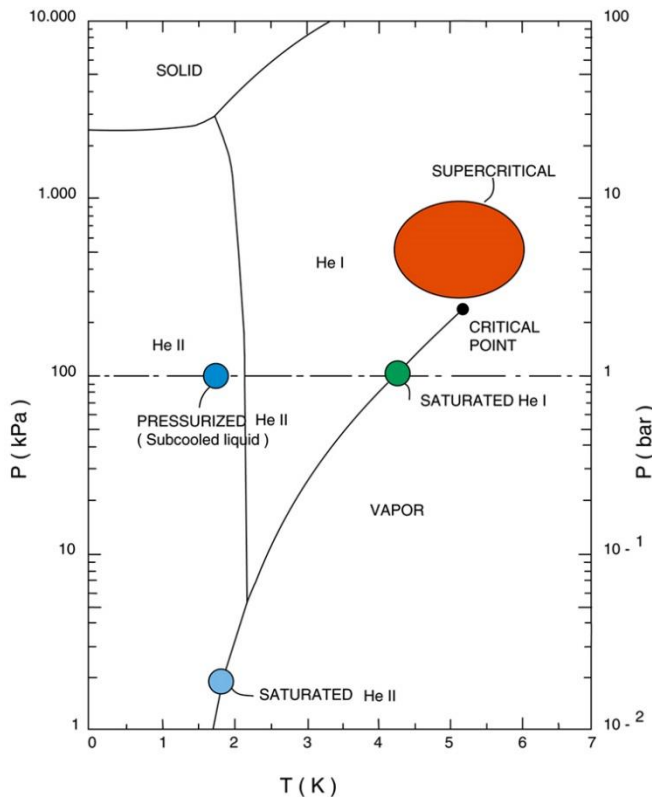
Working domain of saturated helium II is along the saturation line from (starting from 5.0 kPa & 2.17 K, to typically 1.6 kPa & 1.8 K)

Working domain of pressurized helium II, by subcooling liquid at any pressure above saturation, typically near atmospheric pressure (100 kPa).

Additional advantage of functioning in pressurized superfluid helium is that sub-atmospheric pressures are avoided, thus minimizing the impact of air-inleaks, and the good electrically isolating properties (compared with low pressure helium).

Helium as a Advantages of functioning in pressurized superfluid helium w.r.t. saturated helium

Phase diagram of helium



CERN AC - CR106 - 13/03/96

- pressurised helium II can absorb heat, up to the temperature at which the lambda-line is crossed. saturated helium II, which is slightly subcooled due to the hydrostatic head below the surface of the liquid bath, absorbs heat up to the point at which the saturation line is crossed.

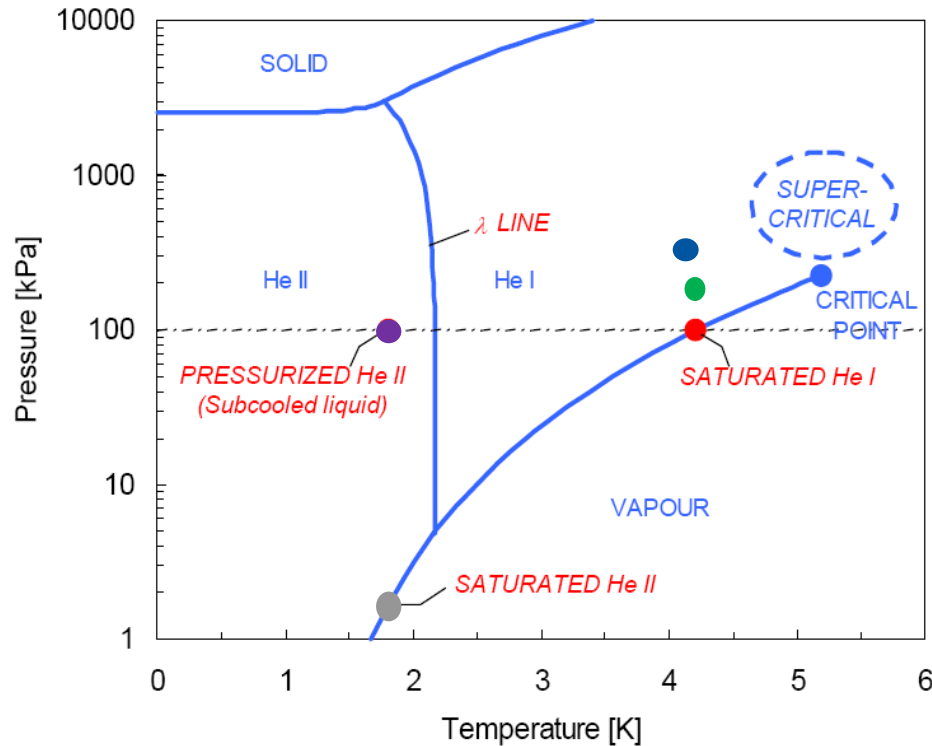
--> The enthalpy difference from the working point to the transition line is usually much smaller in the saturated helium bath. One typically could get an order of magnitude better performance in pressurised helium II (see ref).

- sub-atmospheric pressures are avoided, thus minimizing the impact of air-inleaks.

- both liquids have good electrically isolating properties but low vapour areas, possible when using saturated helium, are prone to electrical breakthrough ("Paschen-curve").

ref: B. Rousset & F. Viargues, *An alternative cooling scheme for the TeV superconducting linear accelerator project*, *Cryogenics 34 ICEC Supplement (1994) 91-94*

Helium as a cold-source: phase-diagram



- SRF -- HERA, LEP, KEKB, CESR
- Magnets -- HERA, Tevatron
- Magnets -- SSC
- Magnets -- Tore Supra, LHC
- SRF -- CEBAF, TTF, SNS, ILC

Listing courtesy Tom Peterson

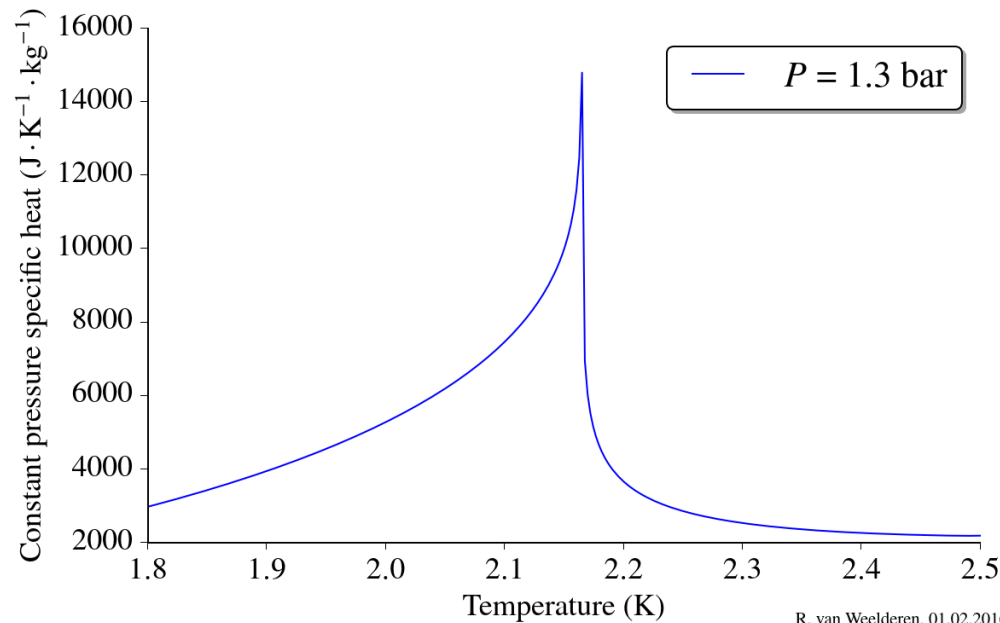
Accelerator magnets are (up to now) often cooled with subcooled liquid

- Typically working near the limit of the superconductor with large stored energy
- Ensure complete liquid coverage and penetration

Superconducting RF cavities are generally (up to now) cooled with a saturated bath

“up to now”: but there’s a drive for several reasons to move most of the liquid out of the system

Intermezzo Hell: Specific heat



C_p of helium

showing the characteristic shape when crossing the superfluid to normal helium transition which gave the transition its name " λ - point"

At these low temperatures, the C_p of helium is roughly at least 4 to 5 orders of magnitude higher than values for coil-pack and collar & yoke materials!

This high thermal capacity of the superfluid helium contributes to coil stability in fully immersed coil magnet designs only at $T < 2.17$ K

Intermezzo Helium Conduction through helium II

Conduction cooling via (pressurized -) superfluid helium can for the majority of heat fluxes and geometries involved in the magnet design $\approx 100 \text{ mW/cm}^3$ be described by the equations for the "turbulent" regime with full mutual friction between the components of the two-fluid model description of superfluid helium.

One uses a simplified superfluid model which is based on a non-linear heat diffusion equation:

$$\rho C_p \frac{\partial T}{\partial t} = \nabla \cdot K_{eff} \nabla T + q_{vol}$$

where ρ is the density q_{vol} is the volumetric heat source and K_{eff} is the non-linear, effective thermal conductivity.

Intermezzo Helium Conduction through helium II

effective thermal conductivity in the turbulent regime (prevalent in the great majority of cases):

$$K_{effT} = \left(\frac{1}{f(T, p) |\nabla T|^2} \right)^{1/3} \quad (1)$$

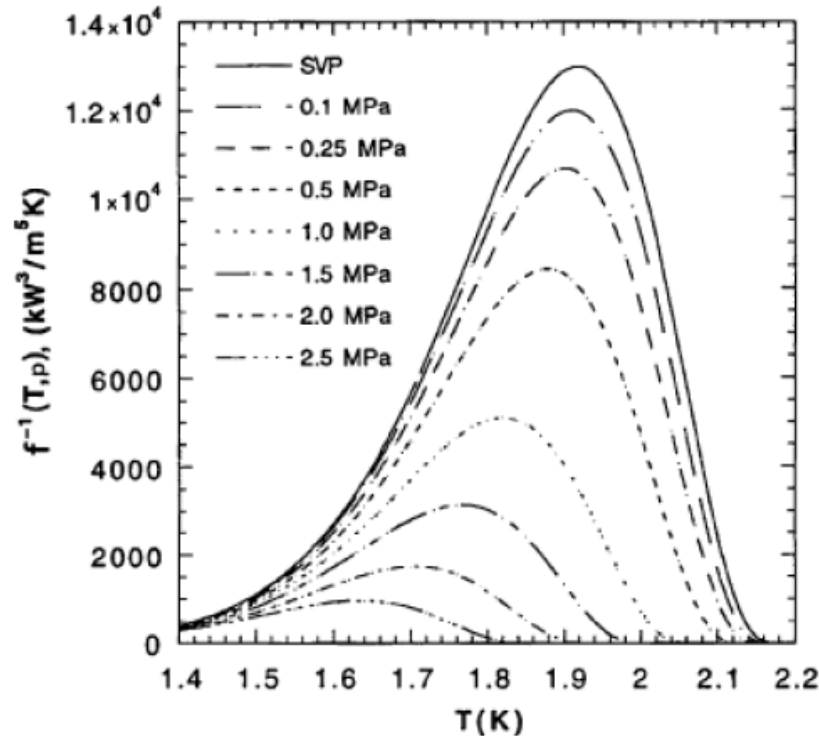
with

$$\frac{1}{f(T, p)} = g(T_\lambda) [t^{5.7} (1 - t^{5.7})]^3 \quad (2)$$

where $t = \frac{T}{T_\lambda}$ and $g(T_\lambda) = \frac{\rho^2 S_\lambda^4 T_\lambda^3}{A_\lambda}$.

S_λ is the reference entropy at the lambda point,
 A_λ is the Gorter-Mellink mutual friction parameter and
 T_λ is the transition temperature from superfluidity at a given pressure.

Intermezzo Helium Conduction through helium II



courtesy van Sciver

Conductivity function

- peaks around 1.9 K
- goes to zero at the lambda-point and for low temperatures

Intermezzo Helium II Conduction through helium II

Inserting $q = -K_{eff}T \frac{dT}{dx}$ in equation (1) we see that the conductivity, although very high, collapses for high heat fluxes

$$K_{eff}T = \frac{1}{f(T, p)q^2}$$

and that the maximum heat flux q^* is limited by channel length L (see exercises)

$$q^* = Z(T_{bath})L^{-1/3}$$

Nevertheless, since $f^{-1}(T, p)$ has values around $1000 \text{ W}^3/\text{cm}^5$, we get for $q = 1 \text{ W}/\text{cm}^3$ an effective conductivity of about $100 \text{ kW}/\text{mK}$. Two orders of magnitude above pure metals at low temperatures.

Intermezzo Helium Conduction through helium II

What makes superfluid helium as a coolant stand-out?

- **high heat capacity**

largely dominates all other cold-mass materials at low temperatures --> increases stability

- **extremely low viscosity**

even within very dense structures, just very low porosity is enough to bring the coolant near the hottest places

- **very good, but functionally special, effective thermal conductivity**

orders of magnitude better than any other cold-mass material

Helium as...: conduction comparative

Normal helium (HeI):

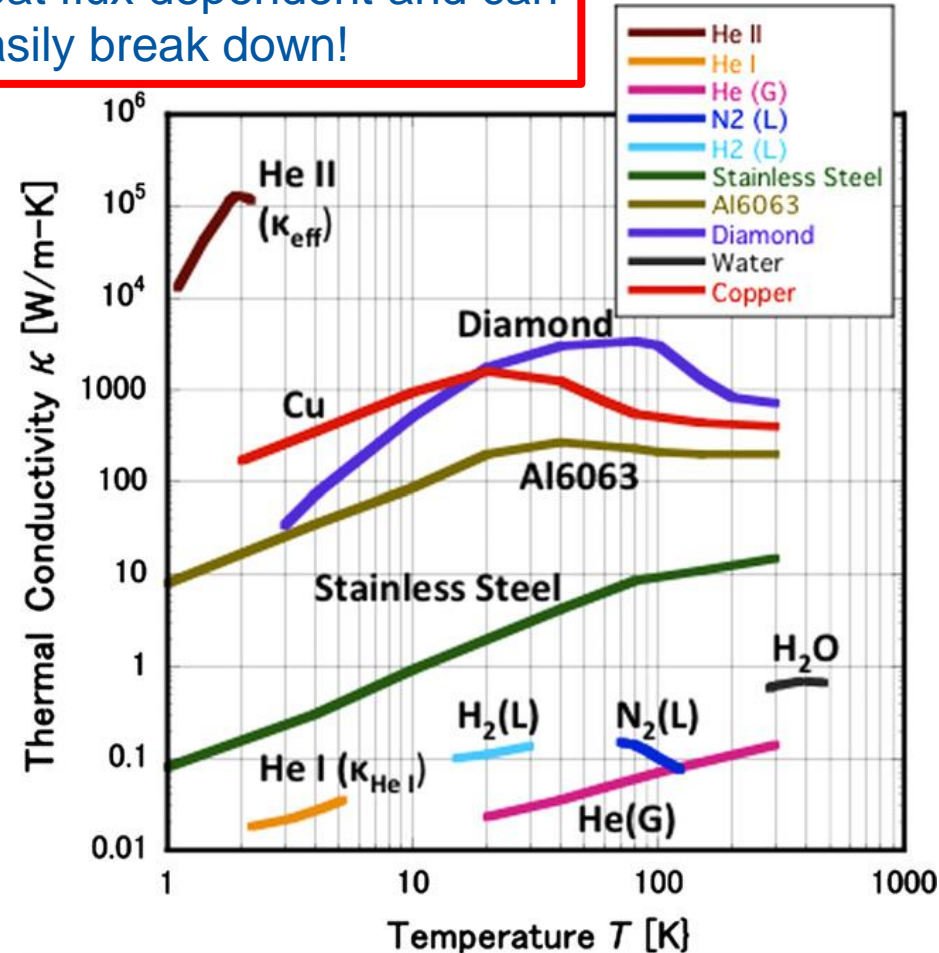
Temperature > 2.17 K
Bad thermal conductivity
Viscous

Superfluid helium (HeII):

Temperature < 2.17 K
Peak in heat capacity c_p at T_λ
High thermal conductivity
Low / vanishing viscosity

- If the *substantially higher refrigeration cost* (see later) can be justified, then HeII is used as a conductive medium
- If not, *then highly conductive materials must be incorporated* in the magnet/coil design to efficiently connect to the cold source

But: HeII conductivity is q^{-3}
heat flux dependent and can easily break down!



Intermezzo: Magnet-examples

Superconducting magnets come in *many variants and applications* ranging from small medical devices, motors, wind-power generators, huge particle detectors and plasma containing structures to km-long particle accelerators,...

The most common superconductors, NbTi, Nb₃Sn, MgB₂, HTS making up the magnet coils *generally operate at temperatures from 1.9 K – 4.5 K – 20 K < 77 K*

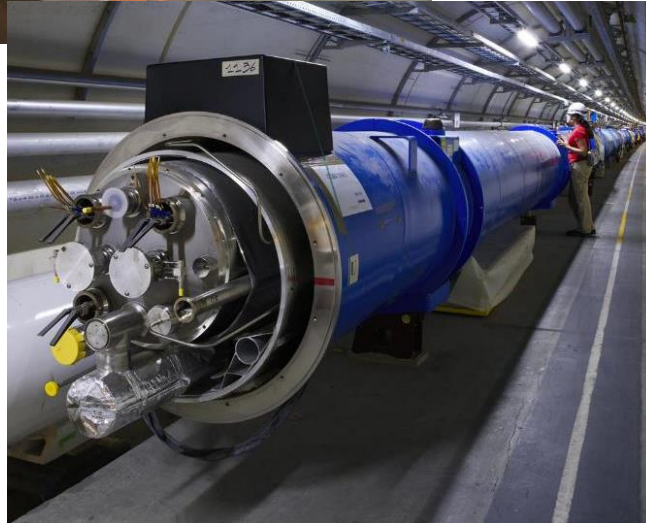
Limiting the heating power from the room temperature environment to reach the low-temperature environment of the coils requires *heat intercepts at intermediate temperatures* (will be quantified later on)

1. The superconducting magnet cryostats typically exhibit a “layered onion – shape”: High temperatures on one side and layers at decreasing temperature levels until the layer that incorporates the superconducting coil.
2. Temperature layers are separated by vacuum spaces to limit heat exchange by gas molecules
3. Mechanical support structures and visible “thermal radiation windows” between these layers are optimized for low heat conduction

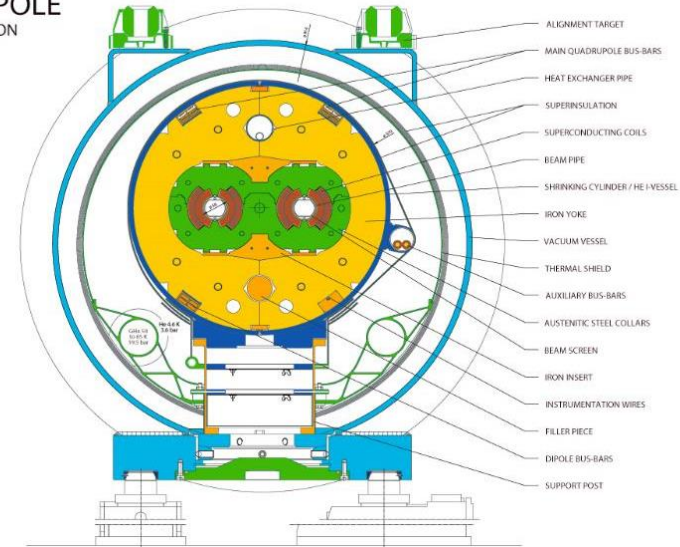
Magnet examples: LHC-particle (proton) accelerator

23 km superconducting magnets **operating @ 1.9 K**, NbTi-cables (HL-LHC upgrade quadrupole → Nb₃Sn)

1232 dipoles, 474 quadrupoles, 7612 corrector magnets

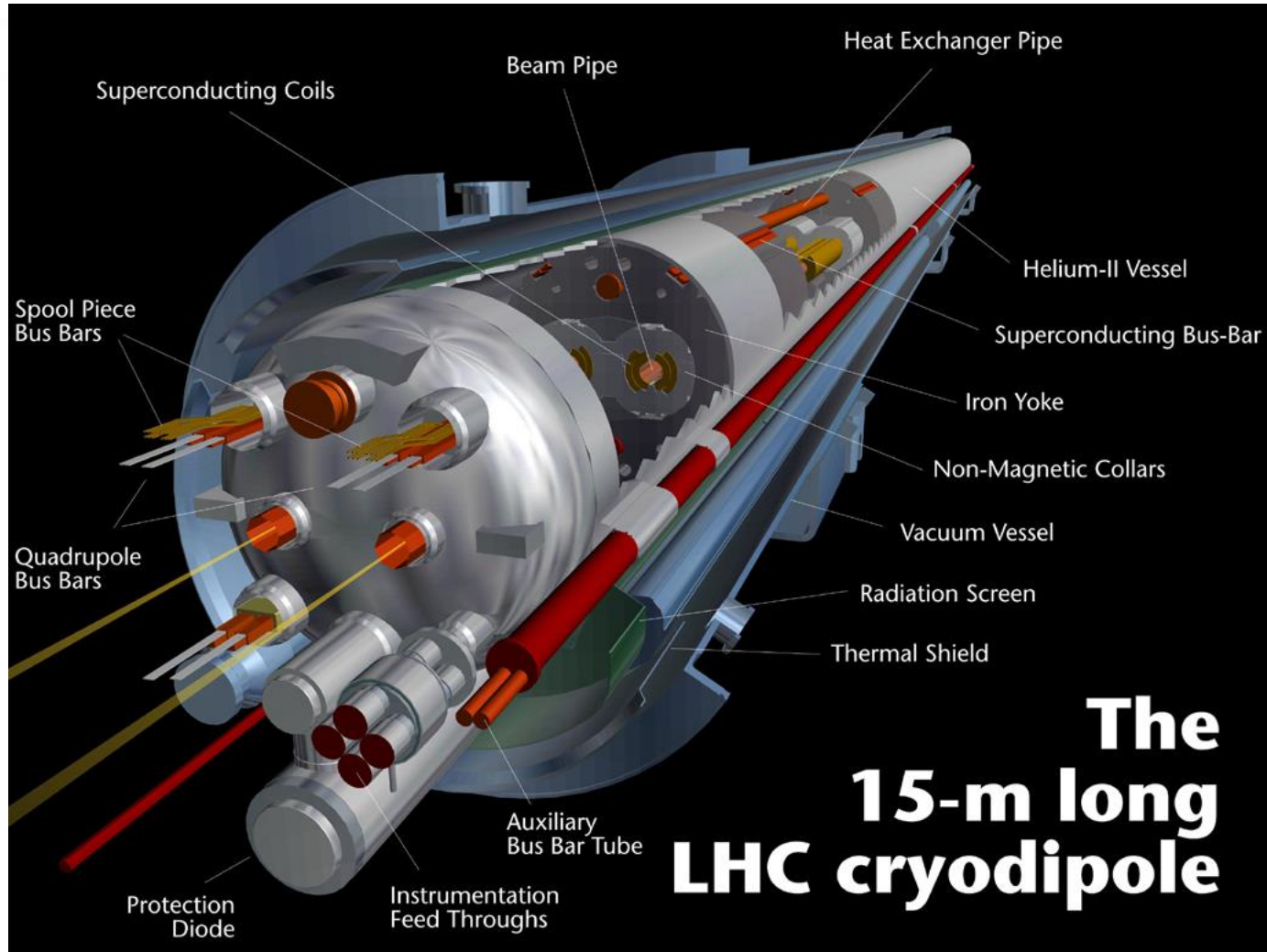


LHC DIPOLE
CROSS SECTION



Fully helium- immersed magnet: coil, collars & yoke all @ 1.9 K (superfluid helium)

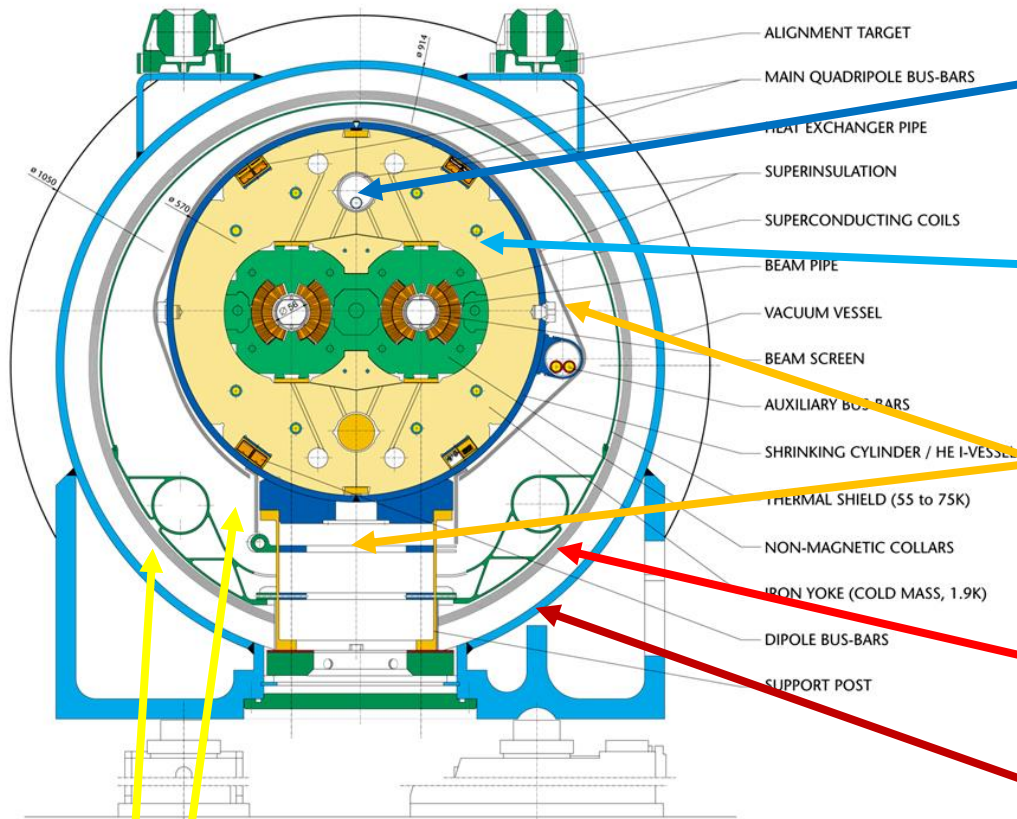
Magnet examples: LHC-dipole



Typical thermal environment & terminology

Magnet examples: LHC-dipole

LHC DIPOLE : STANDARD CROSS-SECTION



T – level (K)	Comment
1.8-2.1	Heat-sink (two-phase superfluid helium)
≤ 2.17	cold -mass (pressurized superfluid helium)
5	Thermal radiation/conduction intercepts
55 - 75	main thermal radiation intercept
RT	outer cryostat shell

CERN AC/DI/MM - HE107 - 30 04 1999

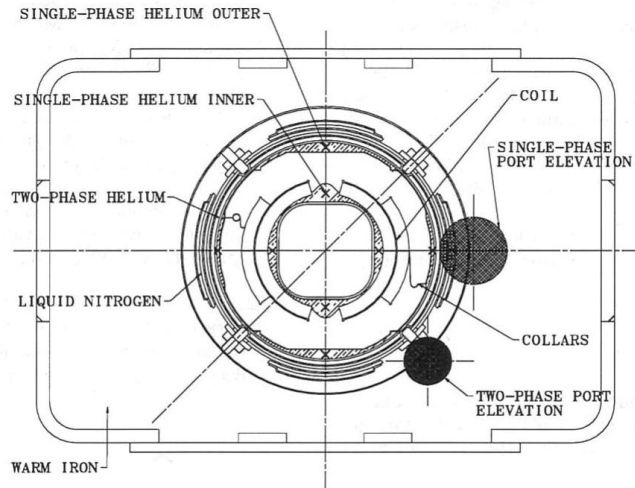
Vacuum spaces

Typical thermal environment & terminology
(example of T-layers)

Magnet examples: Tevatron-particle accelerator

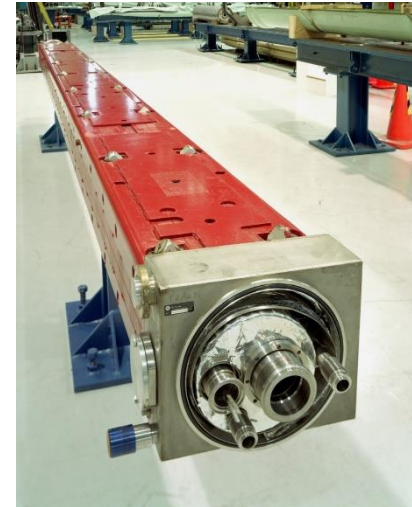
6.5 km of superconducting magnets **operating @ 3.6 Kelvin**, NbTi-cables & warm yoke

+777 dipoles, +216 quads, +204 correction elements



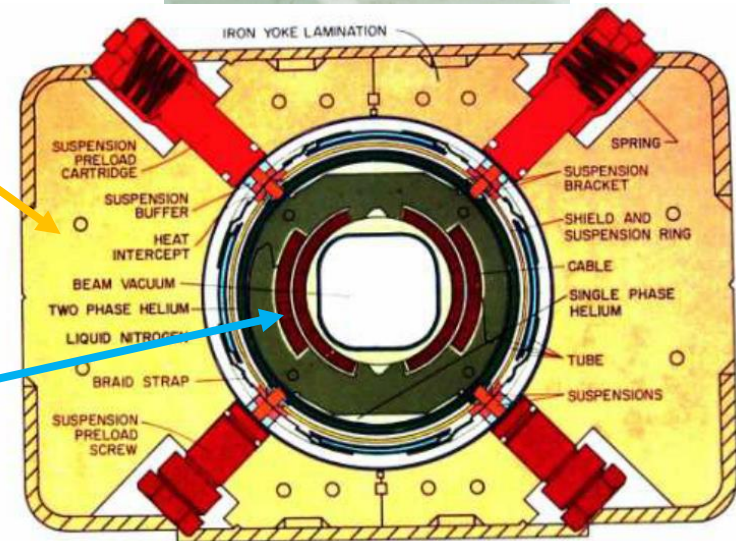
X = SINGLE-PHASE TEMPERATURE SENSOR LOCATION

TEVATRON CROSS-SECTION at SUSPENSION



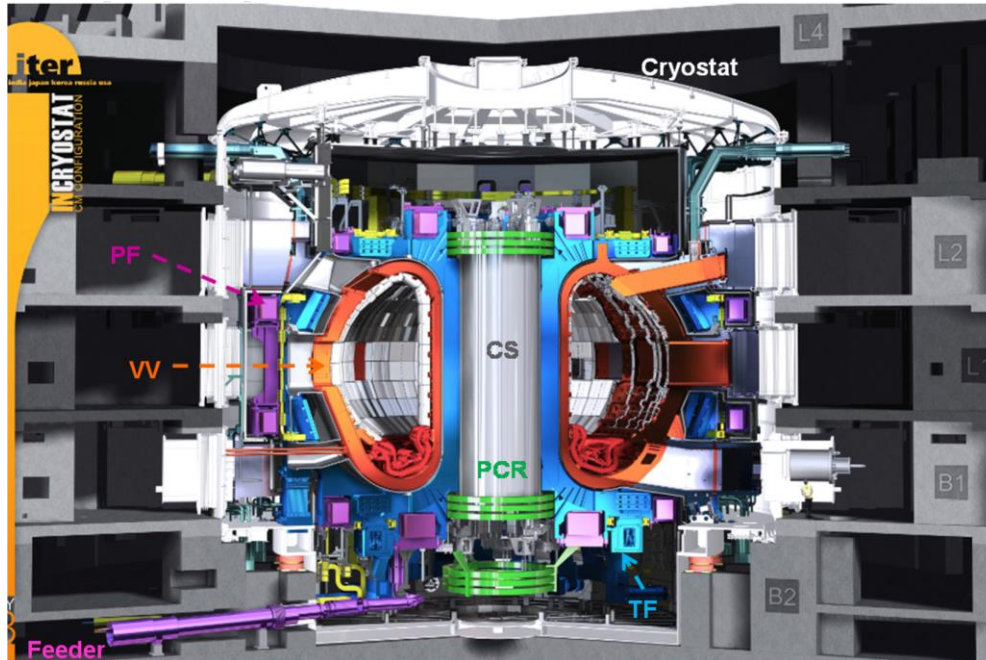
Warm
Yoke

Coil @
3.6 K



Magnet examples: ITER – fusion

Toroidal Field (TF) operating @ 4–6 K force flow cooled K, Nb₃Sn-cables

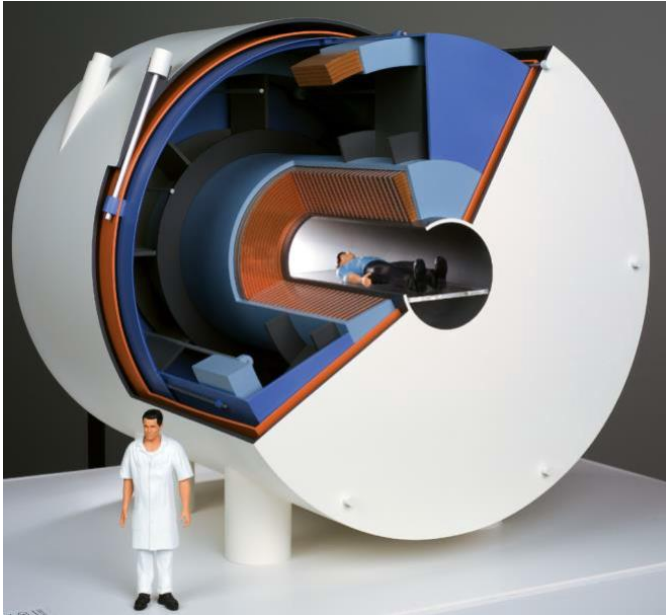


Nb₃Sn, operating at 4-6 K, force flow cooled

<https://www.iter.org/mach/Magnets>

Magnet examples: MRI

CEA/Irfu for NeuroSpin (900mm bore 11.74T 500MHz) magnet



180 km of niobium-titanium superconducting wire wound in double pancake coils and carrying a current of 1,483 A. These superconducting coils are maintained at very low temperatures (1.8 K or -271 °C) using a bath of 5,000 liters of superfluid helium

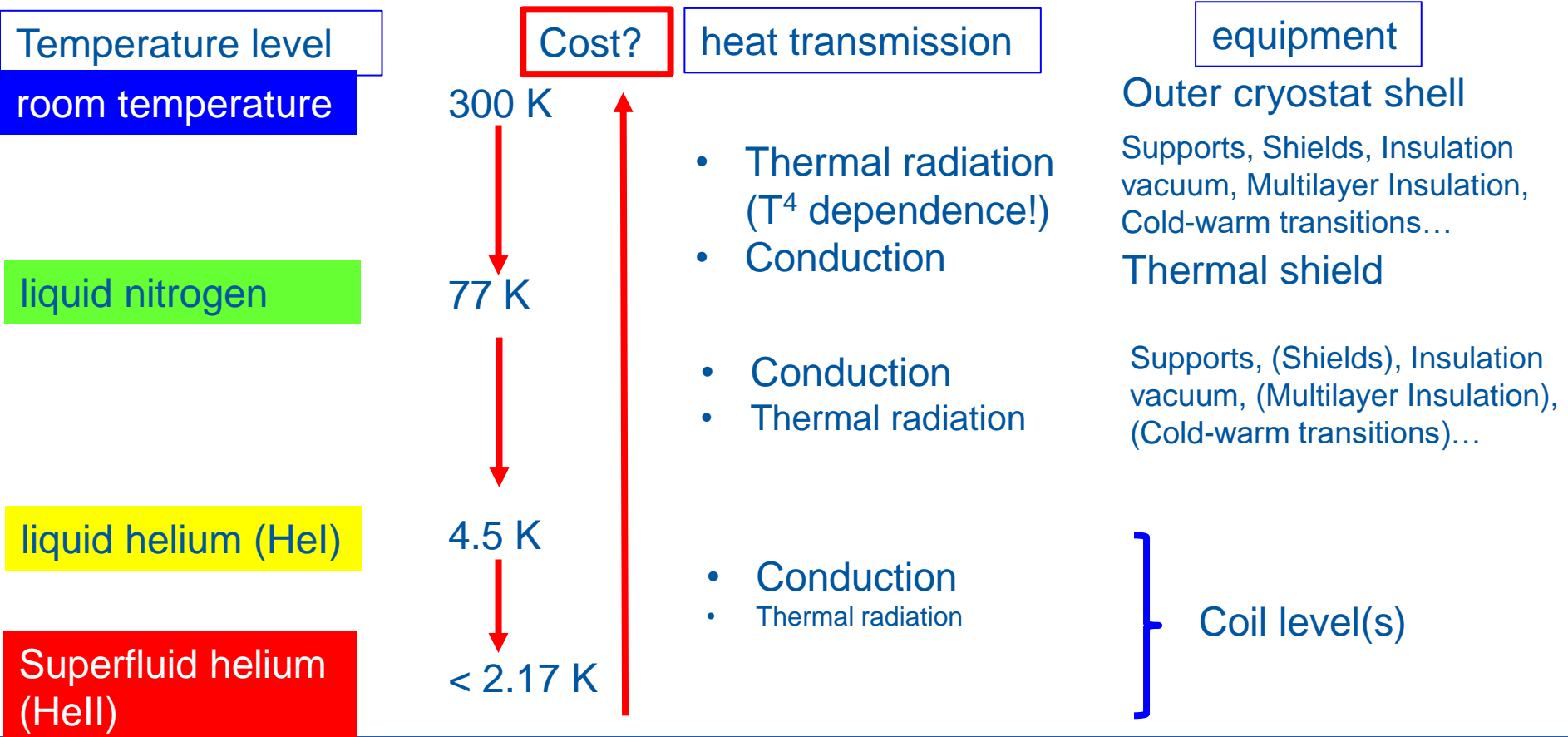
https://joliot.cea.fr/drf/joliot/en/Pages/research_entities/NeuroSpin.aspx

https://irfu.cea.fr/en/Phoce/Vie_des_labos/Ast/ast_visu.php?id_ast=3377

Temperature levels

(and “Why do we need to talk about it?”)

The superconducting magnet cryostats typically exhibit a “layered onion – shape”: High temperatures on one side and layers at decreasing temperature levels until the layer that incorporates the superconducting coil.



Temperature levels

(and “Why do we need to talk about it?”)

In general, cooling is done by using a working fluid, helium in our case (I'll refrain from H_2) and making it undergo a closed thermodynamic cycle that *removes heat at low temperature* (T_{cold}) and rejects the heat at *room temperature* (T_{room}).

This process requires work

Coefficient of Performance COP: the heat absorbed from the cold sink divided by the net work required to remove this heat

Ideally (i.e. thermodynamically reversible process) the “Carnot cycle coefficient”:

$$COP_{ideal} = \frac{1}{\left(\frac{T_{room}}{T_{cold}} - 1\right)}$$

Temperature levels

(and “Why do we need to talk about it?”)

In practice, the inverse (COP^{-1}) is often stated, as this shows the number of watts of work required to provide 1 Watt of cooling at a given temperature:

T_{cold} (K)	COP_{ideal}	COP^{-1}_{ideal} (W/W)
77	0.35	3
4.5	0.015	66
1.9	0.0064	157

!Take with care “Ideal” values” (see next slides)

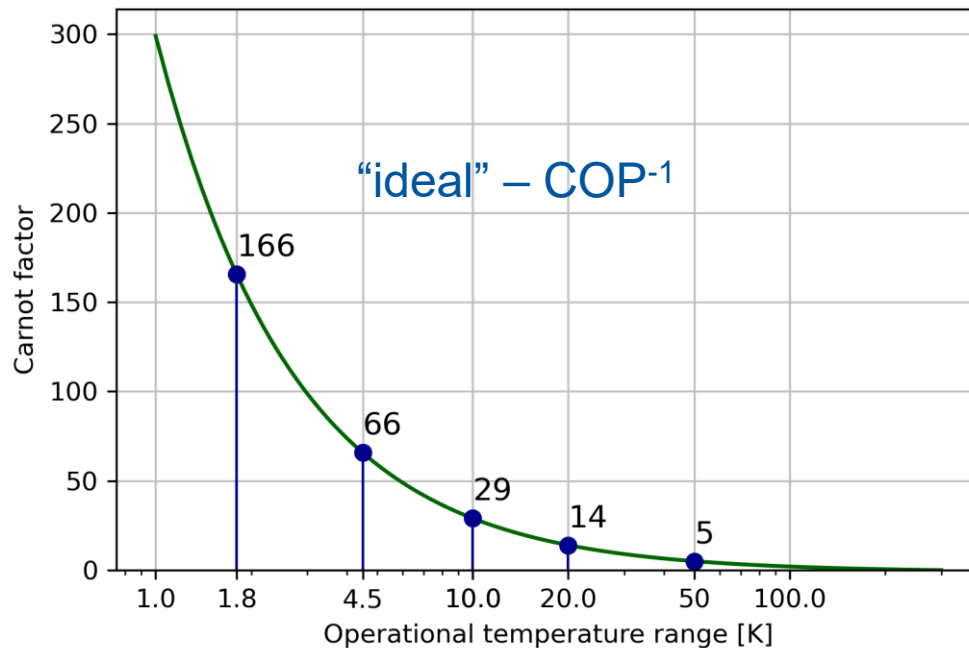
→ it is always thermodynamically more efficient to intercept heat (provide cooling) at higher temperatures!

Temperature levels

(“These values are why we need to talk about it”)

Power consumption at refrigerator I/F

The (*warning!*) “ideal” inverse coefficient of performance (COP^{-1}) power consumption electric power needed per power at cold (W/W).



→ it is always thermodynamically more efficient to intercept heat (provide cooling) at higher temperatures!

Temperature levels

(and “Why do we need to talk about it?”)

In the real world we do not manage to have a cryoplant that operates a fully reversible (ideal) process.

A measure of how good a cryoplant operates is the Figure of Merit (FOM) :

$$FOM = \frac{COP_{real}}{COP_{ideal}}$$

Even the latest LHC cryopplants do not exceed a FOM \approx 30 %

In addition to the non-ideal COP-value one has to add-in a non-negligible power loss to account for the distribution of the coolants (think of pumping losses p.e.). These distribution costs depend heavily on the cooling implementation and are not examined here.

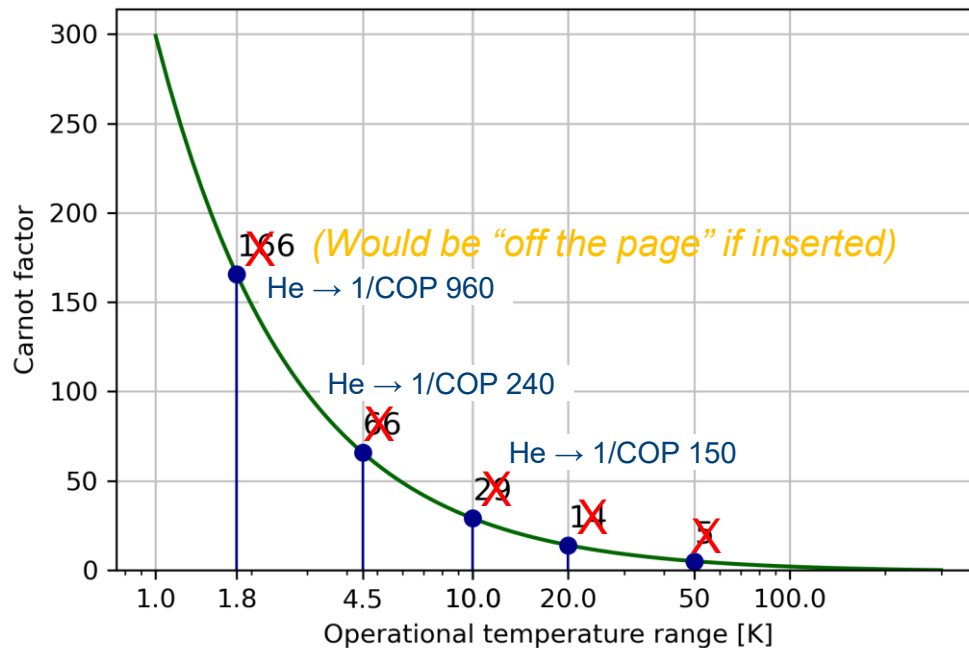
Temperature levels

(“These values are why we need to talk about it”)

Power consumption at refrigerator I/F

From heat loads to power consumption based on actual machine data

The inverse coefficient of performance (COP^{-1}) at refrigerator interface was estimated to give a semi-realistic power consumption.



- Carnot efficiency gives a **potential** reduction in operational costs
 - e.g. from 4.5 K to 10 K there is a **potential** factor 2.3 improvement in efficiency
- But **reality** (process inefficiencies) need to be considered
 - Actual COP at refrigerator interface for 10 K is 150 vs. 240 at 4.5 K → factor 1.6 improvement in efficiency (W/W)
- Losses on distribution and heat extraction systems **still need to be added (up to 30%-50%!)**

Temperature levels

(“These values are why we need to talk about it”)

Power consumption at refrigerator I/F

From heat loads to power consumption based on actual machine data

The inverse coefficient of performance (COP^{-1}) at refrigerator interface was estimated to give a semi-realistic power consumption.

Temperature level	COP^{-1} in $W_{\text{elect}}/W_{\text{cool}}$	FOM (%)	Source
250 K	1		CO ₂ plant ATLAS ITk
100 K	12		LN ₂ plant ATLAS
80 K	16	17	LN ₂ plant ATLAS
20 K	50		20 K/50 kW plot Frey
10 K	150		LHC cryoplant data
4.5 K	240	28	LHC cryoplant data
2.0 K	960	16	LHC cryoplant data

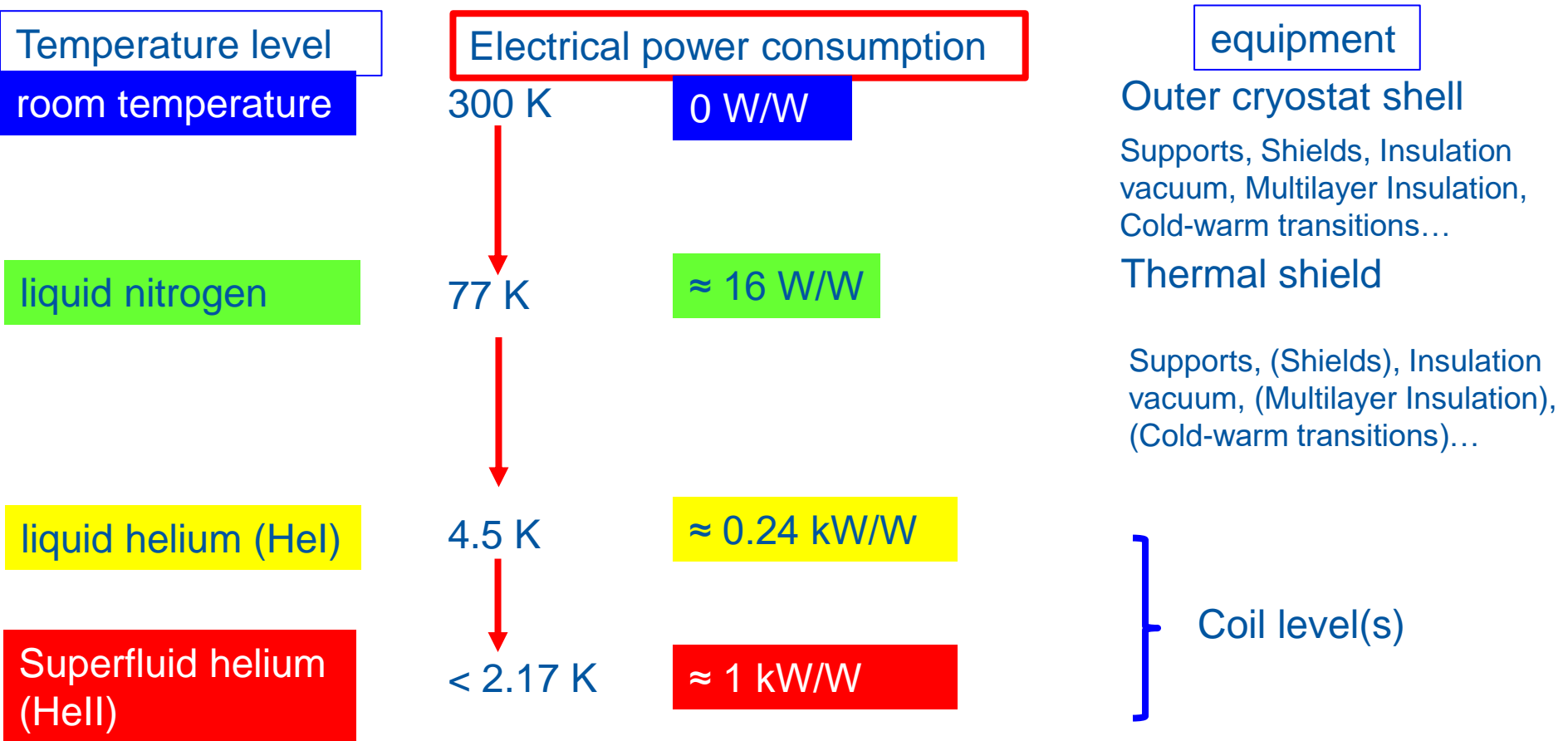
The efficiency of 2.0 K cryoplant wrt 4.5 K goes down much more than you'd estimate from the “ideal” Carnot: from 28 % down to 16 %!

→ Be careful not to fully rely power consumption-scaling, when changing temperatures, on ideal Carnot coefficient ratios!

$\approx 1 \text{ kW/W @ 2.0 K !}$
 $\approx 0.24 \text{ kW/W @ 4.5 K}$

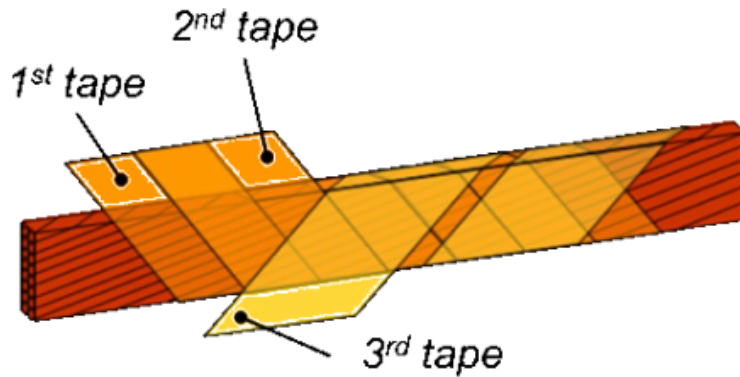
Temperature levels

(“These values are why we need to talk about it?”)



Take away: try to incorporate in the magnet design, whenever possible, features to intercept heat at as high T as possible!

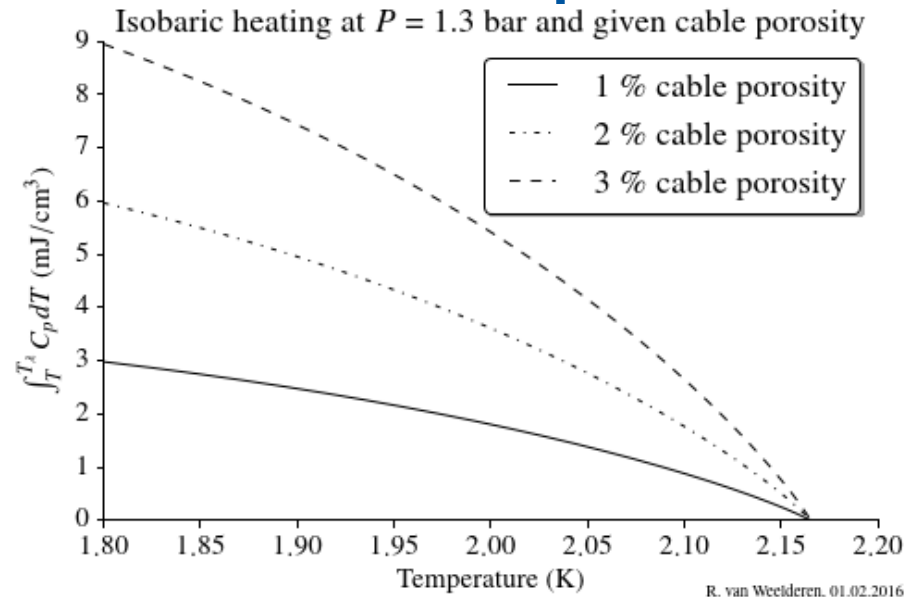
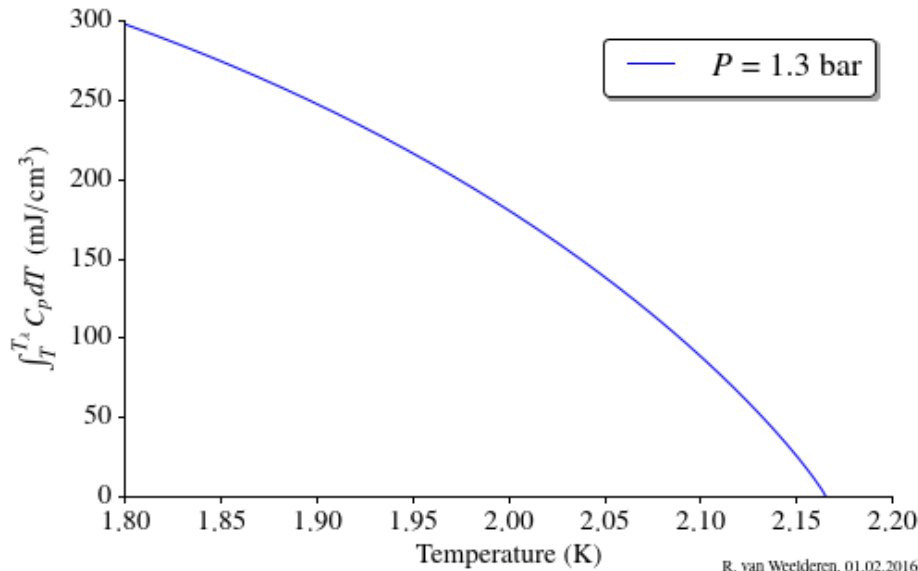
Fully immersed in Hell: LHC-dipoles



NbTi - cable is:

- non-impregnated
- Electrically insulated by partially overlapping layers of Kapton
- > porous to helium

Fully immersed in Hell: LHC-dipoles



The high thermal capacity of the helium inside the porous NbTi - cable contributes to the stability

The order of magnitude is ~ 2 mJ/cm³ per % of He volume

To be compared with typical assumed quench stability margin of NbTi at $T < 2.17$ K of ~ 5 -10 mJ/cm³

Heat sources and heat-sinks

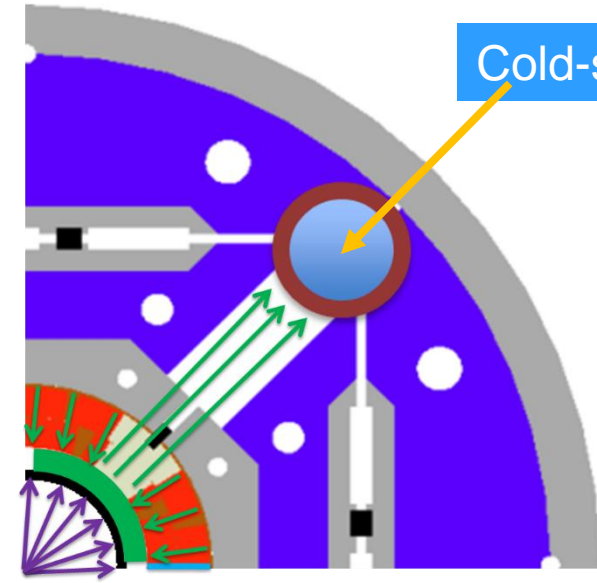
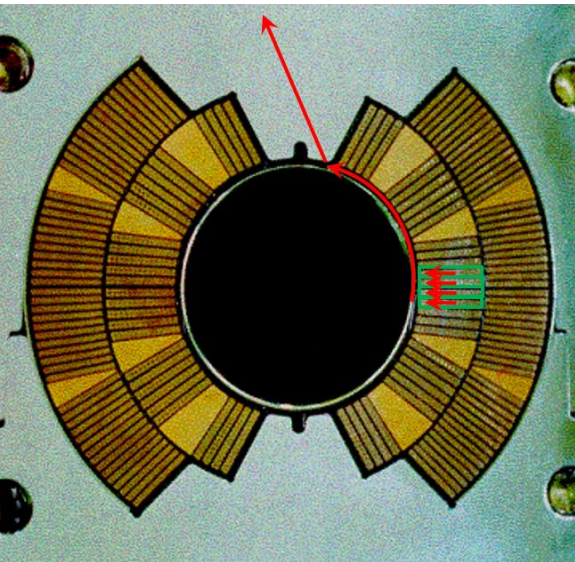
(aka “cold-sources”)

In *fully immersed* magnets the heat generated in the coil-pack must find its way out to the cold-source via helium path-ways kept clear in the cold-mass construct

In the example top left, of the LHC main dipole, heat flows from the coil pack into the annular space between beam-pipe and coil-pack and out via space between the collar laminations

Cold-source

In the example bottom left, of the HL-LHC MQXF quadrupole, heat flows from the coil pack into the annular space between beam-pipe and coil-pack and out via dedicated passages (8 mm diameter holes every 50 mm along the length of the magnet)

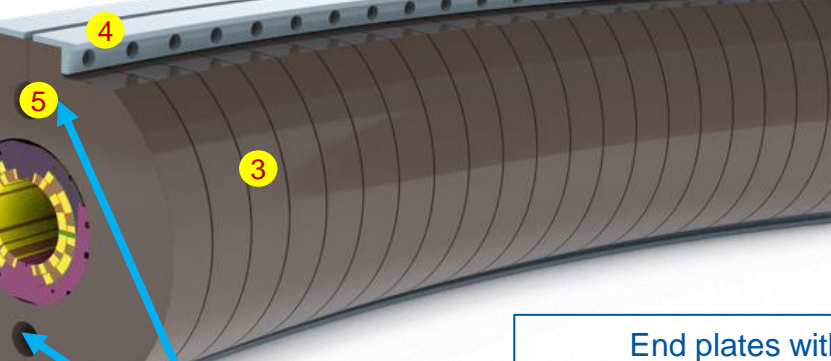


(aka “cold-sources”)

In a “dry” magnets the heat generated in the coil-pack must find its way out to the cold-source via solid conduction and solid-liquid interface

Technical drawing of a circular mechanical part, likely a rotor or stator component. The drawing shows a cross-section with various dimensions and labels:

- Dimensions:**
 - Outer diameter: $\varnothing 70$
 - Inner diameter: $\varnothing 66.5$
 - Inner hole diameter: $\varnothing 66$
 - Radial thickness: 12.5
 - Segment width: 18.5
 - Segment height: 14.5
 - Segment angle: 24°
 - Segment angle: 52°
 - Segment angle: 65°
- Labels:**
 - 1**: Points to the outer ring.
 - 2**: Points to the inner ring.
 - 3**: Points to the central hole.
 - 4**: Points to the inner ring.
 - 5**: Points to the outer ring.
 - 6**: Points to the inner ring.
 - 7**: Points to the outer ring.
 - 8**: Points to the inner ring.
 - 9**: Points to the outer ring.
 - 10**: Points to the inner ring.
 - 11**: Points to the outer ring.
 - 12**: Points to the inner ring.
 - 13**: Points to the outer ring.
 - 14**: Points to the inner ring.
 - 15**: Points to the outer ring.
 - 16**: Points to the inner ring.
 - 17**: Points to the outer ring.
 - 18**: Points to the inner ring.
 - 19**: Points to the outer ring.
 - 20**: Points to the inner ring.
 - 21**: Points to the outer ring.
 - 22**: Points to the inner ring.
 - 23**: Points to the outer ring.
 - 24**: Points to the inner ring.
 - 25**: Points to the outer ring.
 - 26**: Points to the inner ring.
 - 27**: Points to the outer ring.
 - 28**: Points to the inner ring.
 - 29**: Points to the outer ring.
 - 30**: Points to the inner ring.
 - 31**: Points to the outer ring.
 - 32**: Points to the inner ring.
 - 33**: Points to the outer ring.
 - 34**: Points to the inner ring.
 - 35**: Points to the outer ring.
 - 36**: Points to the inner ring.
 - 37**: Points to the outer ring.
 - 38**: Points to the inner ring.
 - 39**: Points to the outer ring.
 - 40**: Points to the inner ring.
 - 41**: Points to the outer ring.
 - 42**: Points to the inner ring.
 - 43**: Points to the outer ring.
 - 44**: Points to the inner ring.
 - 45**: Points to the outer ring.
 - 46**: Points to the inner ring.
 - 47**: Points to the outer ring.
 - 48**: Points to the inner ring.
 - 49**: Points to the outer ring.
 - 50**: Points to the inner ring.
 - 51**: Points to the outer ring.
 - 52**: Points to the inner ring.
 - 53**: Points to the outer ring.
 - 54**: Points to the inner ring.
 - 55**: Points to the outer ring.
 - 56**: Points to the inner ring.
 - 57**: Points to the outer ring.
 - 58**: Points to the inner ring.
 - 59**: Points to the outer ring.
 - 60**: Points to the inner ring.
 - 61**: Points to the outer ring.
 - 62**: Points to the inner ring.
 - 63**: Points to the outer ring.
 - 64**: Points to the inner ring.
 - 65**: Points to the outer ring.
 - 66**: Points to the inner ring.
 - 67**: Points to the outer ring.
 - 68**: Points to the inner ring.
 - 69**: Points to the outer ring.
 - 70**: Points to the inner ring.
 - 71**: Points to the outer ring.
 - 72**: Points to the inner ring.
 - 73**: Points to the outer ring.
 - 74**: Points to the inner ring.
 - 75**: Points to the outer ring.
 - 76**: Points to the inner ring.
 - 77**: Points to the outer ring.
 - 78**: Points to the inner ring.
 - 79**: Points to the outer ring.
 - 80**: Points to the inner ring.
 - 81**: Points to the outer ring.
 - 82**: Points to the inner ring.
 - 83**: Points to the outer ring.
 - 84**: Points to the inner ring.
 - 85**: Points to the outer ring.
 - 86**: Points to the inner ring.
 - 87**: Points to the outer ring.
 - 88**: Points to the inner ring.
 - 89**: Points to the outer ring.
 - 90**: Points to the inner ring.
 - 91**: Points to the outer ring.
 - 92**: Points to the inner ring.
 - 93**: Points to the outer ring.
 - 94**: Points to the inner ring.
 - 95**: Points to the outer ring.
 - 96**: Points to the inner ring.
 - 97**: Points to the outer ring.
 - 98**: Points to the inner ring.
 - 99**: Points to the outer ring.
 - 100**: Points to the inner ring.



End plates with axial location of coil ends (not shown)

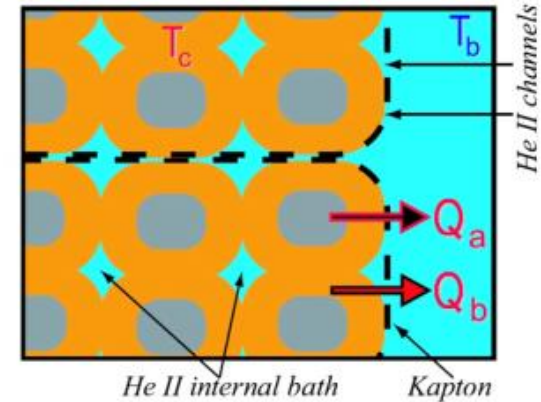
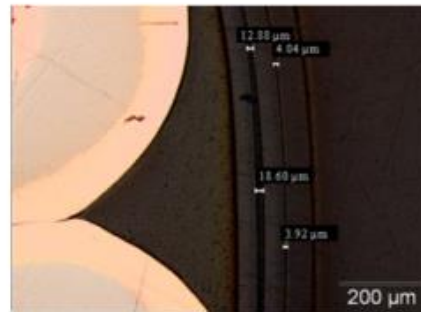
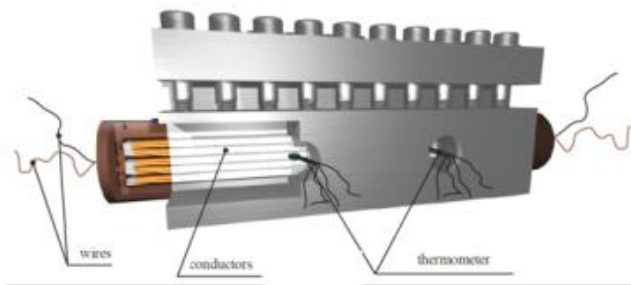
End plates with axial loading
of coil ends (not shown)

Heat sink(s)

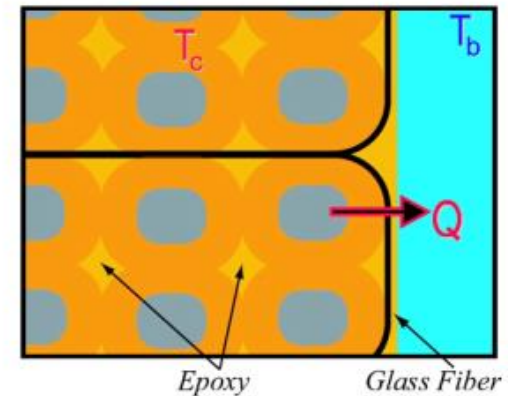
Fully immersed in Hell



Cable T excursions w.r.t. helium bath measured as function of power deposit



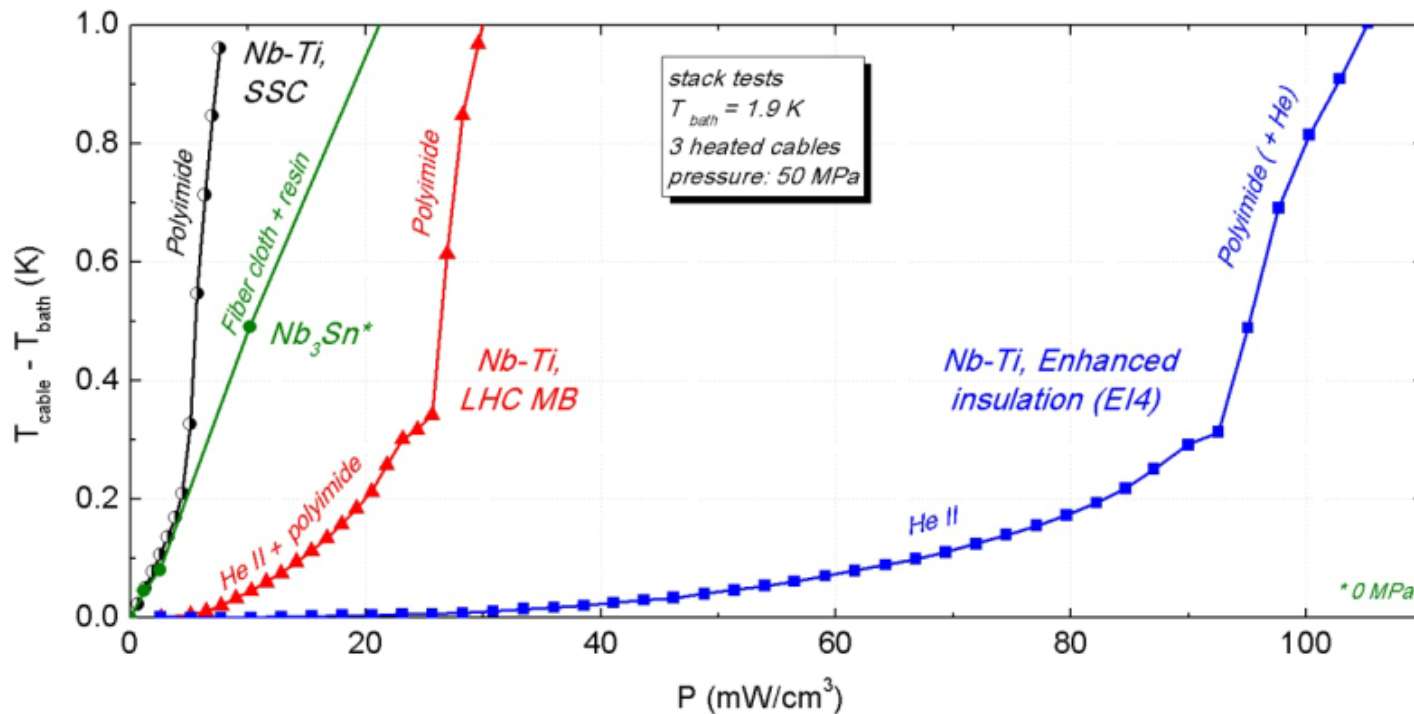
NbTi cables showing the porosity w.r.t. helium



Nb₃Sn cables, fully impregnated, only conduction through solids

courtesy H. R. Correia Rodrigues

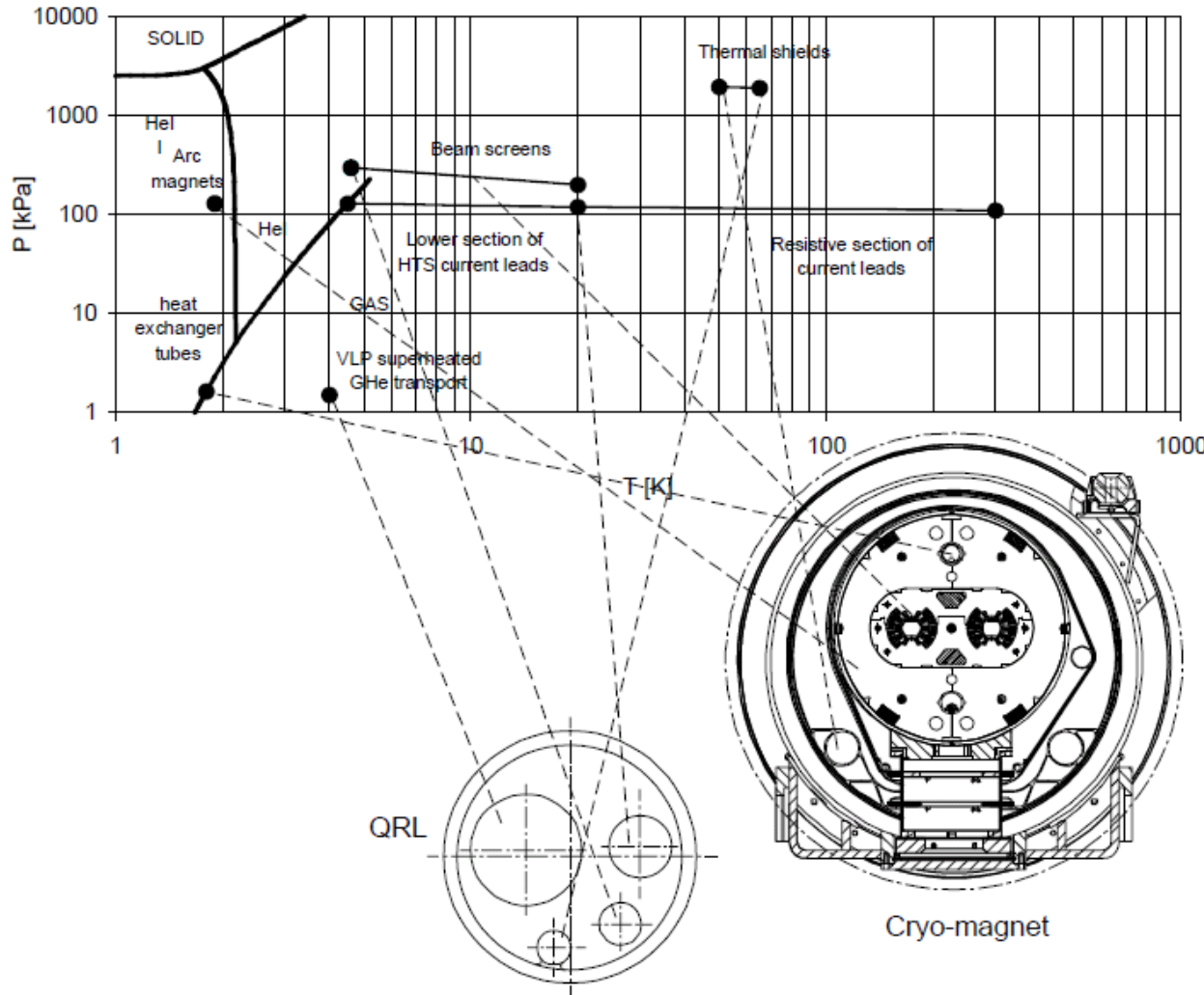
Fully immersed in Hell



Stack measurement results, all faces open, showing the stark difference between porous and fully impregnated cables

Nb₃Sn measurements have since, the last 5 years, been addressed in more detail (see [3])

Fully immersed in Hell: LHC-dipoles

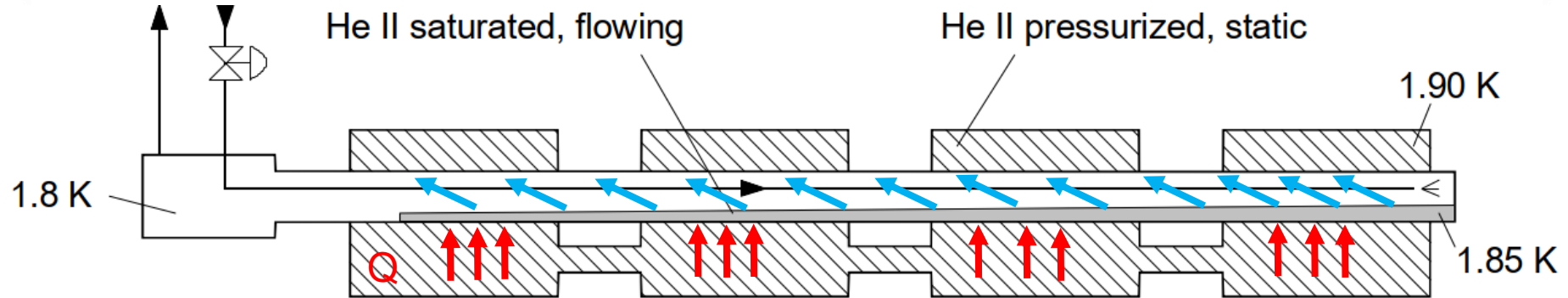


Addressing yesterday's question:

Even if the coil, collar and yoke are in pressurized Hell at 1.3 bar and ~ 1.9 K

The heat-sink (upper hole), where the heat is taken up by vapourizing liquid helium (~ 1.85 K, ~ 15 mbar) is in a copper-pipe protruding over the length of several magnets (107 m)

Fully immersed in HeII: LHC-dipoles



All the extracted heat has eventually to flow across the tube wall, where it encounters three thermal impedances in series:

- the limited solid conduction across the metal constitutive of the wall,
- the Kapitza resistances produced by the refraction of thermal phonons at the metal-to-helium interfaces.

The overall transverse impedance was measured on fully wetted test samples at varying temperature, so that the different temperature dependence of the solid conduction and Kapitza terms enabled to resolve them. For tubes with a wall thickness up to about 1 mm, the Kapitza resistance largely dominates below 2 K, and the use of high-purity, cryogenic-grade copper is not required.

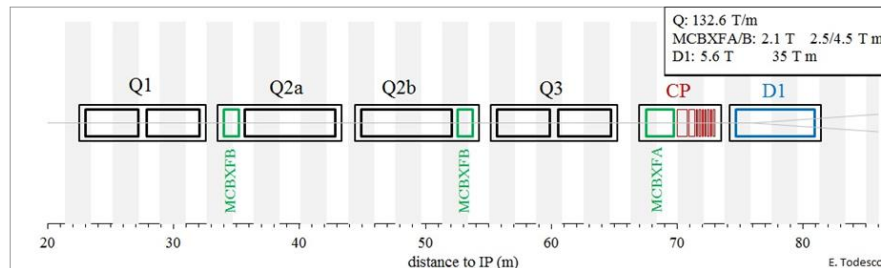
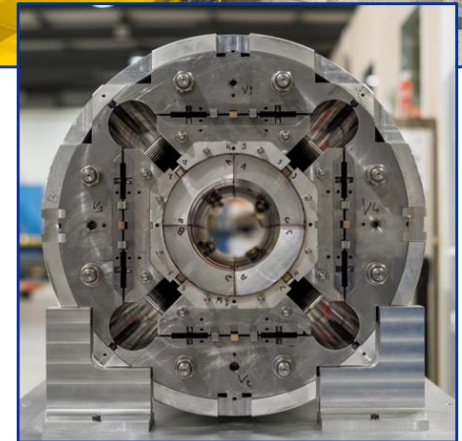
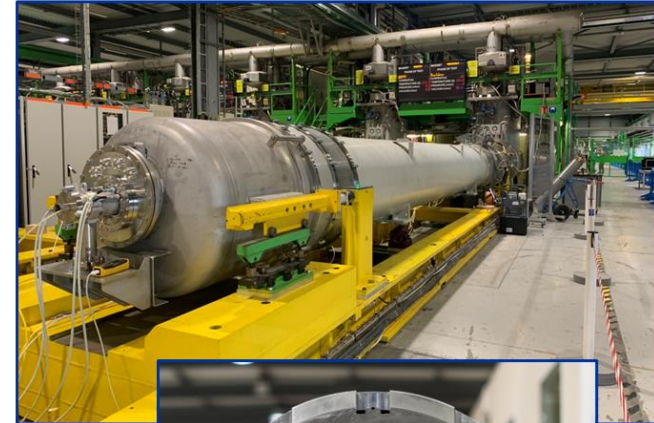
See ref[1, 2]

Evaporation of two-phase, very low pressure, helium flow

Fully immersed in Hell: MQXF

(HL-LHC Nb_3Sn quadrupoles)

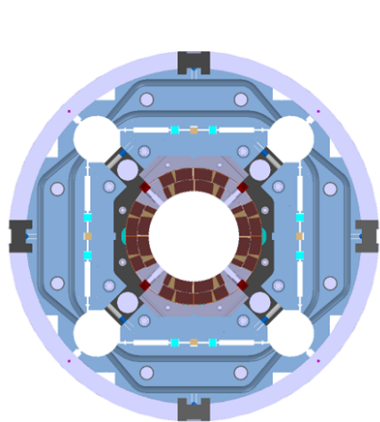
- In the context of HL-LHC at CERN, **a robust multi-region CFD numerical framework** for the modelling of **heat transfer in complex cryogenic system geometries involving He II** has been developed
- Numerical tool allowed to **provide thermal design requirements early enough in the magnets' design phase**
- Now, **a fully upgraded and consolidated tool** is used to reassess previous results, and for systematic analysis of heat extraction pathways in complex He II – composite solid geometries



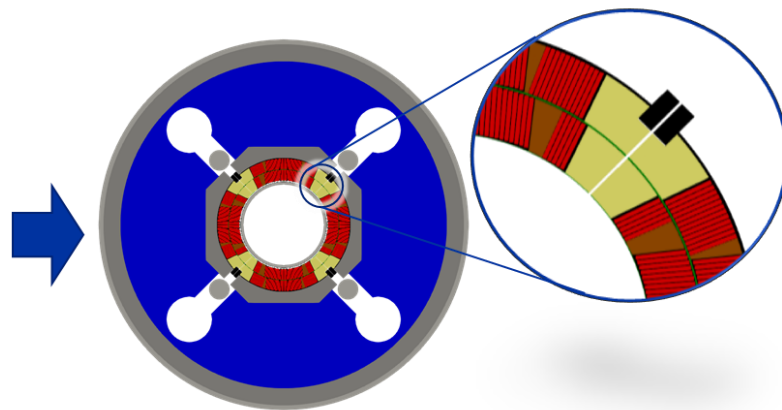
Following slides: courtesy P. Borges de Sousa | Revised estimates of temperature margins in MQXF, see also ref[x]

Numerical code applied to full-scale cold masses

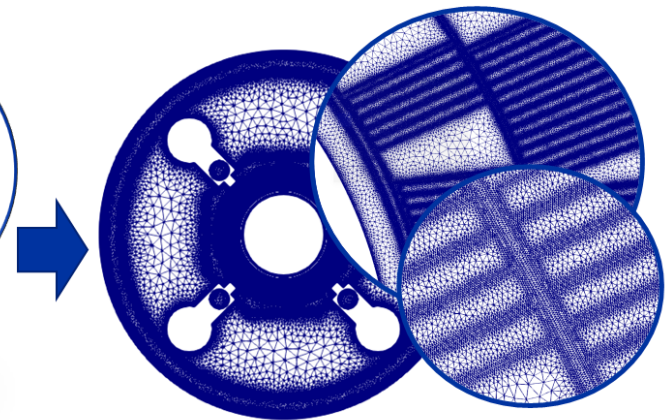
- **Libraries and solver** implemented in OpenFOAM v7, **geometry** created via Python API for Salome, easily adjustable for **parametric studies**
- Currently handles **2D geometries** and **static He II conditions** (no flow) and **He II \rightarrow He I transition**
- **Power deposition data** can be mapped directly onto the geometry, or **direct heat input** to any part
- **Coil described in detail**; mesh composed of 3.5M cells, **special refinement on thin layers**



MQXF v7 + cold mass
(ST0703448)

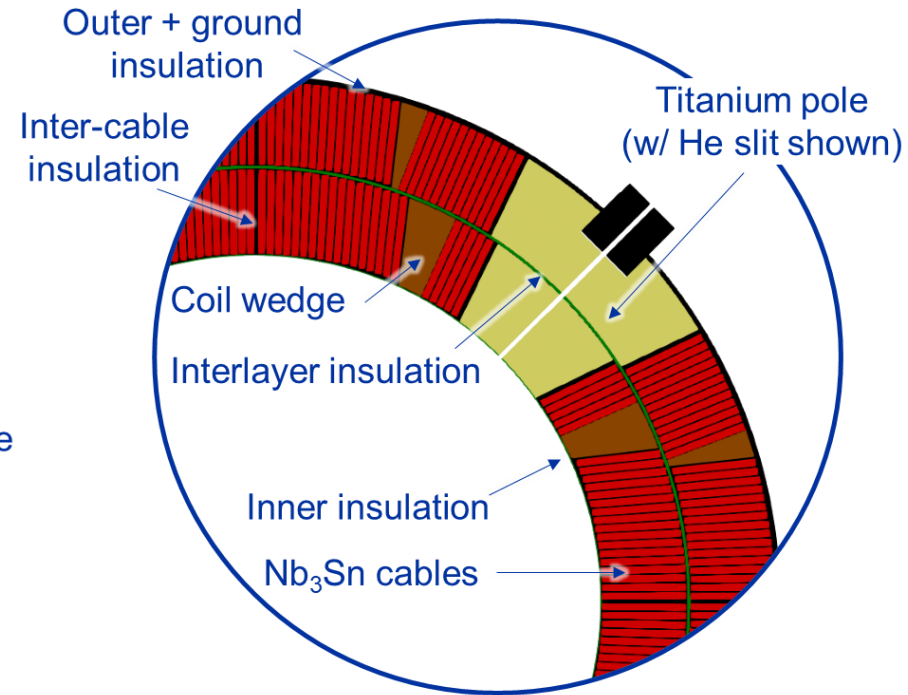
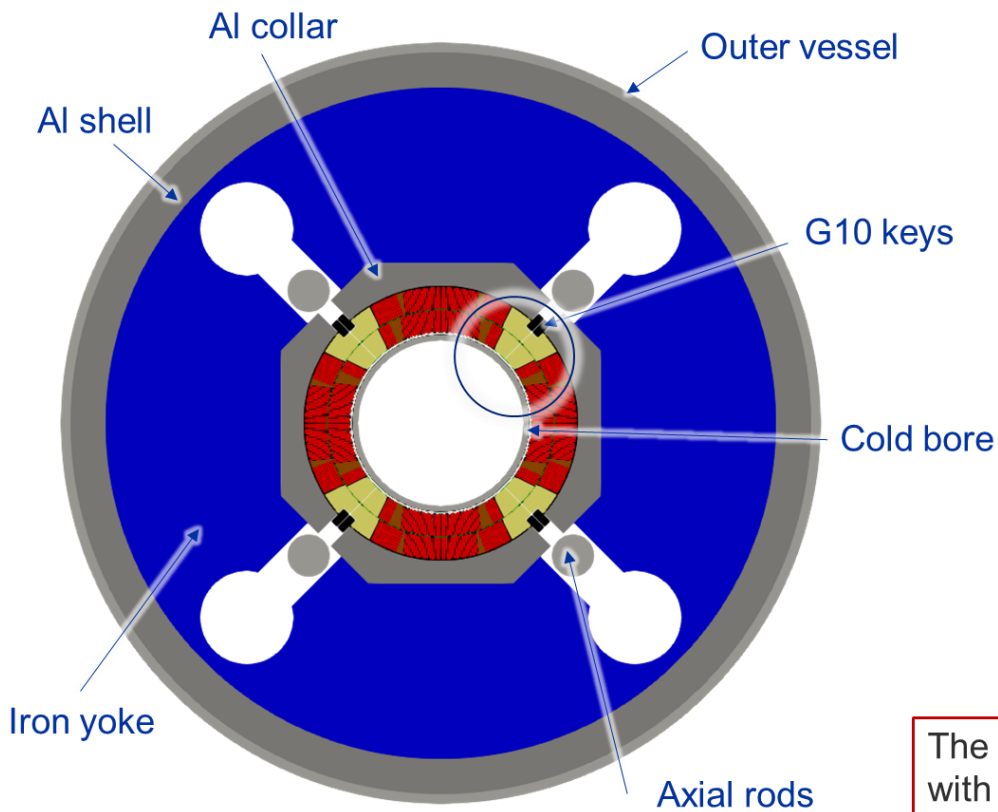


Simplified geometry for simulation
(coded in Python and Salome)



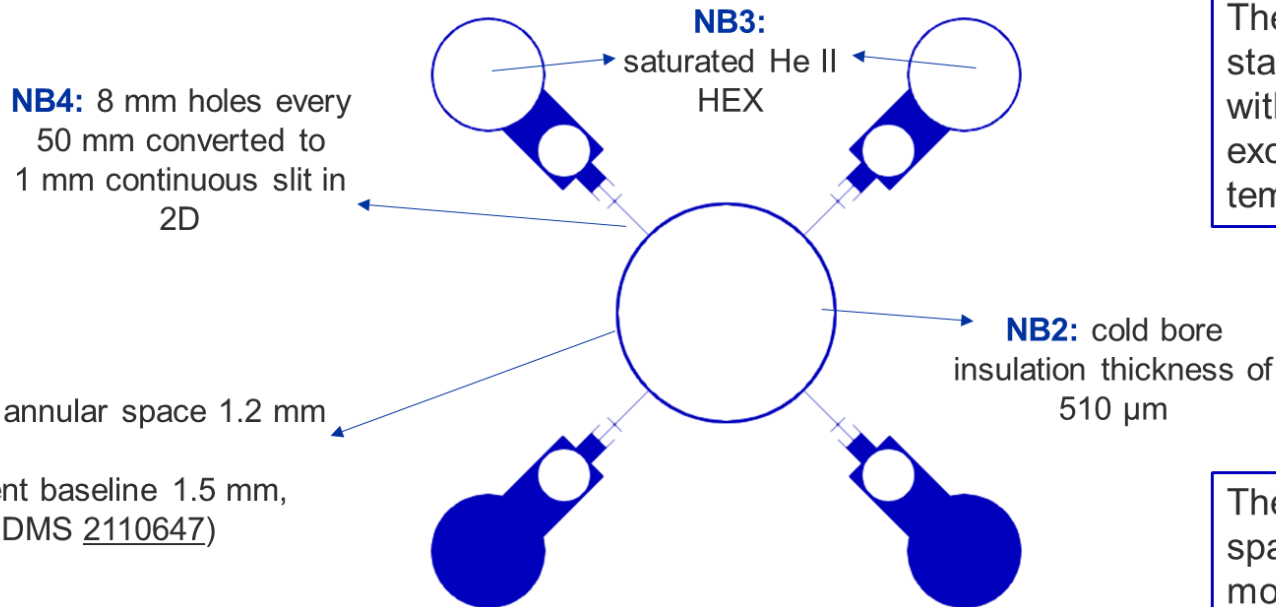
Resulting 2D meshed geometry
(coded in Python and Salome)

MQXF cold mass geometry – composite solid



The **solid region** is composed of 17 different zones, each with their own temperature-dependent material properties

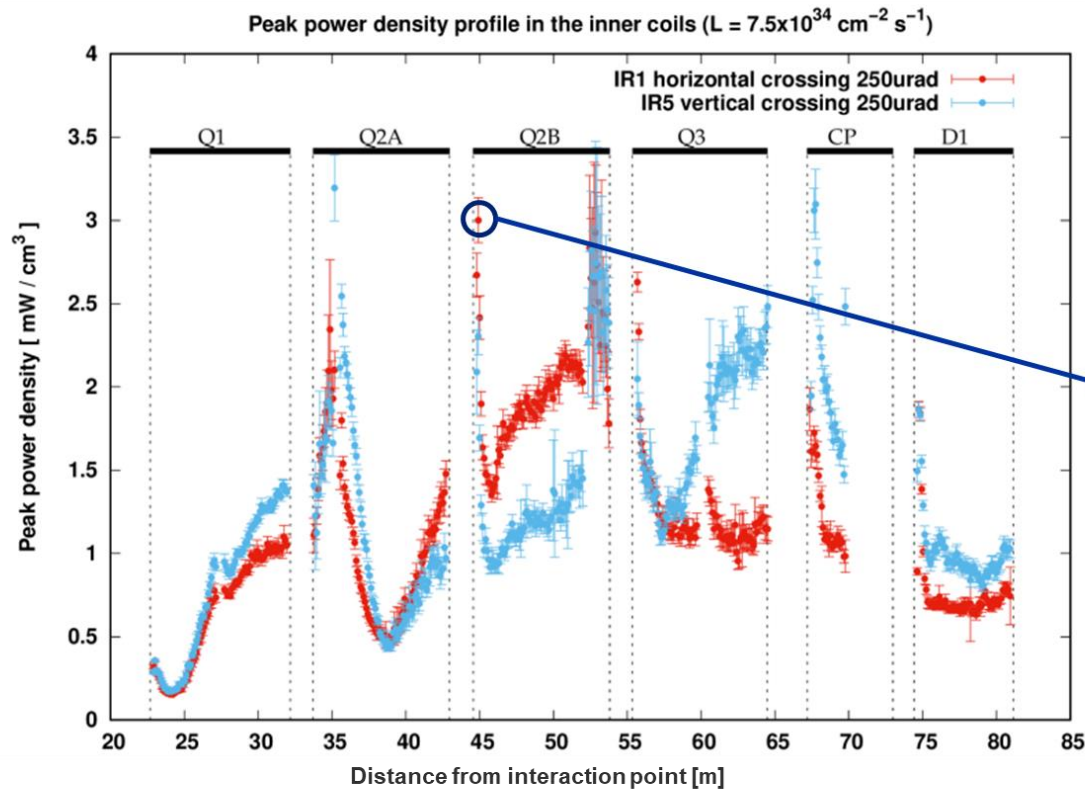
MQXF cold mass geometry – He II region



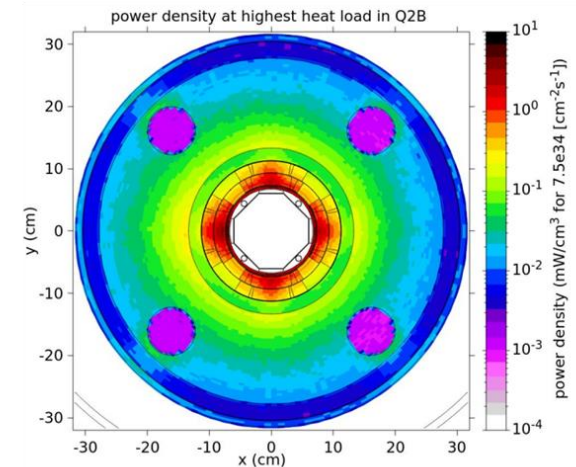
The **He II region** is modelled as a static pressurised bath in contact with the saturated He II heat exchangers at a constant temperature

The connection between annular space and HEX passages is modelled as a continuous 1 mm slit over the cold mass' length

Input for heat deposition from dose calculations (I)



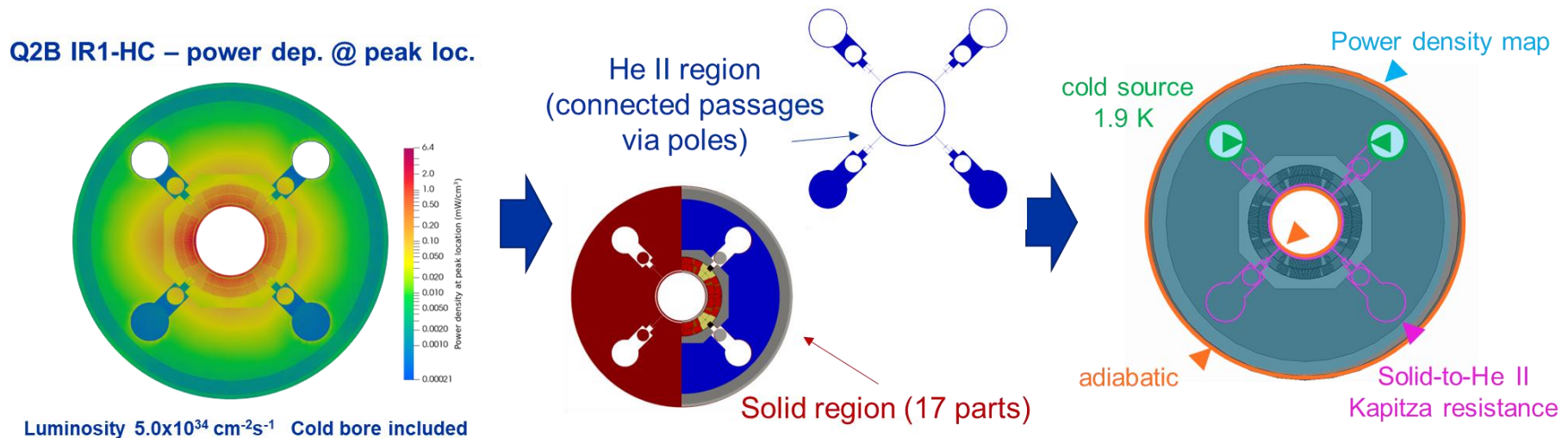
- For each magnet/cold mass, **the cross-section that corresponds to the highest dose** (and consequently heat load) is selected
- 12 cross-sections selected** (Q1/2/3A and B, vertical and horizontal crossings)



Source: [Review of estimates of energy deposition, M. Sabate-Gilarte](#)

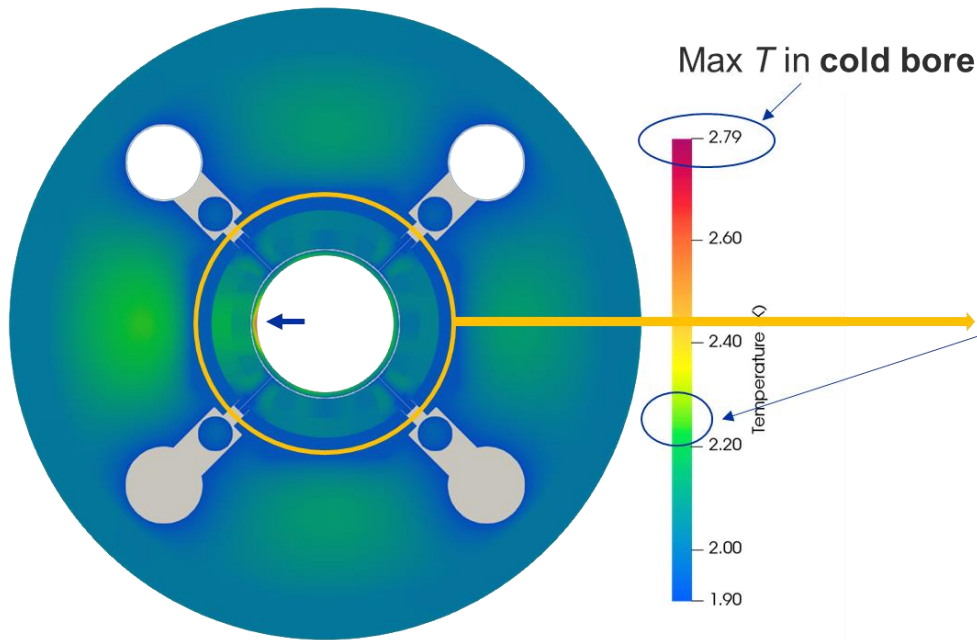
Input for heat deposition from dose calculations (II)

- For each cold mass, the 2D **power density** (mW/cm³) **at the peak** (maximum) **location** for nominal luminosity (7 TeV, 5.0×10^{34} cm⁻²s⁻¹) is mapped onto the mesh
- Mesh is split into two regions, a **He II region** and a **solid region**
- Set of **boundary conditions** is chosen; power density map changes for every analysed cross-section

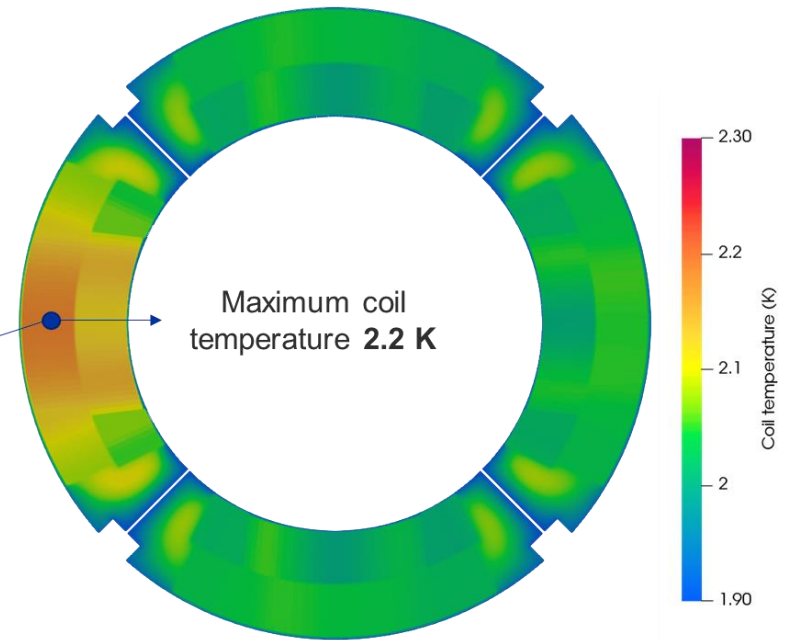


Results: example Q2B IR1-HC @ nominal luminosity

Temperature distribution at peak location

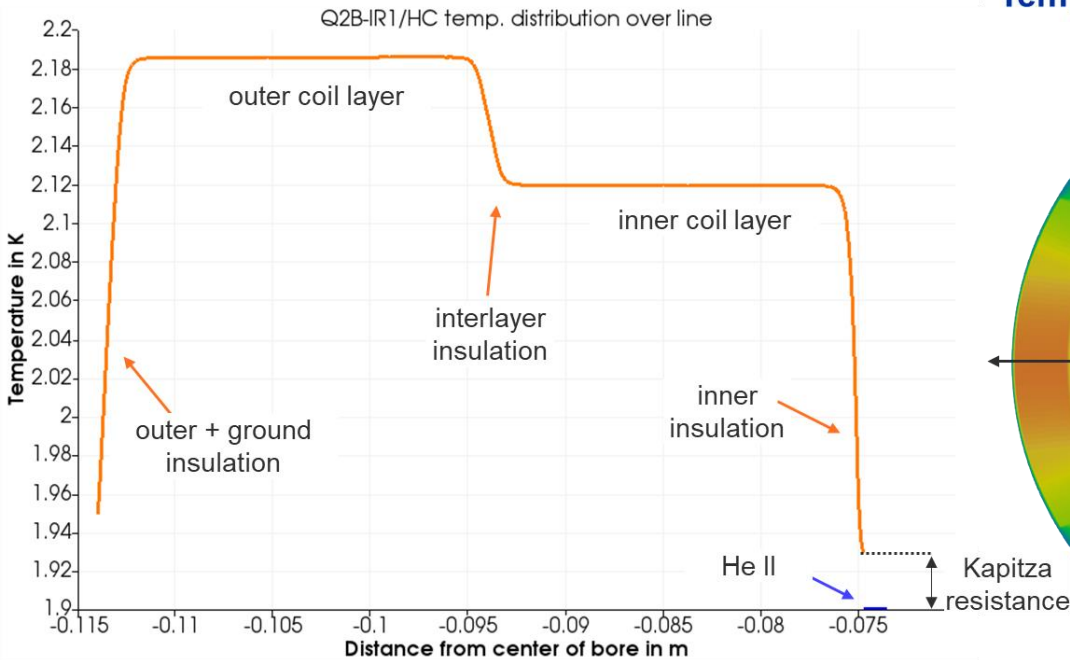


Temp. distribution at peak location (coil detail)

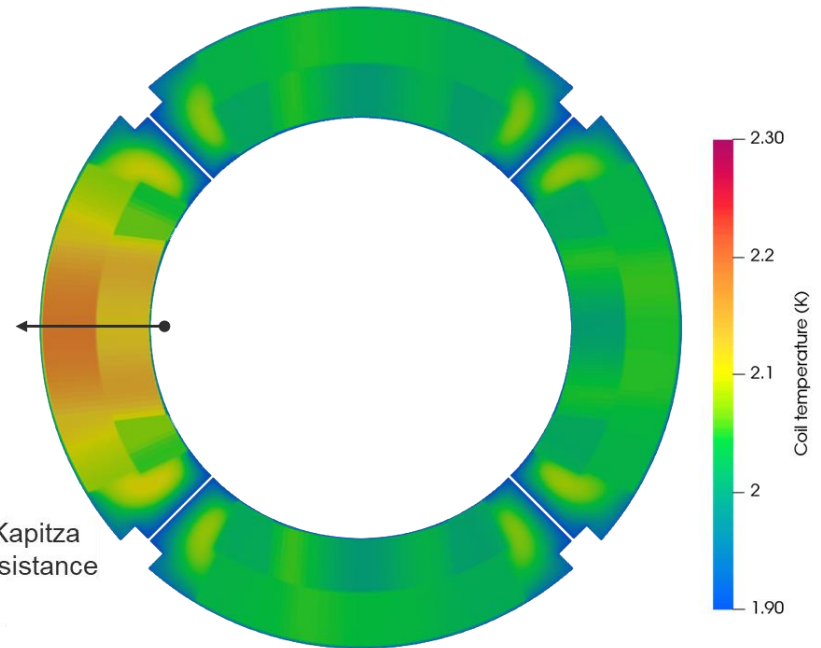


NB: Cold bore included, luminosity = $5.0 \times 10^{34} \text{ cm}^{-2}\text{s}^{-1}$

Results: example Q2B IR1-HC @ nominal luminosity



Temp. distribution at peak location (coil detail)



With fully impregnated cables, the thermal gradients are mainly determined by the interfaces (in contrast with NbTi-helium permeable cables)

With fully impregnated cables, the thermal gradients *are mainly determined by the interfaces* (in contrast with NbTi-helium permeable cables)

→ Going from fully helium-immersed coils to “dry” conduction-cooled coils is for fully impregnated cables, apart from an additional DT, a similar situation.

For future magnet development based on fully impregnated coils the temperature gradient ΔT across the coil must be kept as low as possible:

- Control the interfaces
 - Electrical insulation (Kapton foils p.e.)
 - Quench heaters (external, CLIQ, inductive...)
 - New impregnation materials (can we enhance the conductivity & Cp?)
- New conductors
 - Anisotropy of HTS tapes
 - Electrically insulated or non-insulated HTS tapes
 - ...
- Conductivity & Cp data of new magnet designs to be measured
 - Accurate data greatly detailed thermal analysis

Key takeaways

- A **robust, easily adaptable numerical framework** has been consolidated to evaluate heat extraction mechanisms in **complex cryogenic system geometries involving He II**
- We are now able to produce results in a timeframe that allows for **parametric investigation of geometry, operational T , and power deposition** on magnet systems cooled by static, pressurised He II → this enables a **systematic approach**, and **can be used as a tool in magnet design** w.r.t. heat extraction
- Numerical simulations **directly benefit from the material data obtained from the experimental test campaign**, allowing for **more realistic, accurate calculations**
- The **heat extraction pathways for the HL-LHC inner triplet magnets have been validated** for the latest geometry, considering a steady-state power deposition at peak location for nominal operating conditions ($5.0 \times 10^{34} \text{ cm}^{-2}\text{s}^{-1}$, 7 TeV), at 1.9 K cold source

ASC 2022 paper submitted to IEEE Transactions on Applied Superconductivity (TAS)

Numerical Assessment of the Inhomogeneous Temperature Field and the Quality of Heat Extraction of Nb₃Sn Impregnated Magnets for the High Luminosity Upgrade of the LHC

Patricia Borges de Sousa, Kirtana Puttina, Maria Shahn-Gilani, Francesco Cerutti, Susana Inguero Bermudez, Enzo Todesco, Rob van Weelden

Abstract—The High Luminosity upgrade of the Large Hadron Collider (HL-LHC) at CERN foresees the installation of Nb₃Sn-based quadrupole magnets at selected interaction points of the accelerator. The precise knowledge of each magnet's thermal characteristics and heat extraction performance is essential to power deposition during both nominal and ultimate conditions in order to determine safe operating margins. A 2D numerical framework has been developed to systematically assess the temperature distribution in the combined magnet structure-superfluid He system of each magnet and converging cold mass using open-source software. Here a full cross-section of a magnet coil mass is modelled, under the power density distribution expected at the most exposed longitudinal position during accelerator operation at the nominal conditions for the HL-LHC. Temperature maps and margins are presented for the inner triplet magnets (MQXF) for both horizontal and vertical beam crossing conditions, along with the validation of the design of cold mass cooling channels for heat extraction.

Index Terms—cryogenics, numerical simulation/model, power deposition, Nb₃Sn magnets, Helium II, HL-LHC

I. INTRODUCTION
In the context of the High-Luminosity upgrade of the LHC at CERN, a robust multi-scale CFD numerical tool using open-source software for the modelling of heat transfer in complex cryogenic system geometries involving He II has been developed, aiming to provide thermal design requirements [1] early enough in the design phase of the inner triplet magnets, such that they could be implemented in the mechanical design.
Previously established temperature margins along the full cross-section of inner triplet cold masses need to be updated to reflect changes in both power deposition by beam collisions

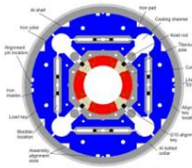


Fig. 1. Representative cross-section of the HL-LHC inner triplet quadrupole magnet cold mass (MQXF) [1].

debris and coil layout, and to validate the best extraction design that was originally proposed.
The work presented here is a continuation of previous studies [2]–[4], implementing updated MQXF geometry, power density maps and experimentally-obtained material properties, as well as a fully upgraded numerical tool that enables a systematic analysis of multiple magnet cross-sections and allows for parametric studies in a timely manner.
To model the temperature distribution in the combined solid-superfluid He system of each cold mass, the numerical tool itself and the 2D magnet model framework have been greatly refined. The model now includes seamless He II – He I phase-transition and converges more than an order of magnitude faster.
II. GEOMETRY AND NUMERICAL TOOL
A. Geometry of MQXF cold mass
A 2D cross-section of a MQXF quadrupole magnet cold mass representative of the cold mass' single section, along with the cold bore (see Fig. 1), was created according to the

every 50 mm along the magnet axis and that connect the inner He II annulus space between the cold bore and the inner radius of the coil to the cooling channels, a continuous 1 mm slit along the maximum pole and G10 alignment key was created to enable a 2D geometry with equivalent longitudinal cross-section (see detail in Fig. 2 (a)).
Each component of the cold mass is assigned appropriate temperature-dependent material properties such as density, specific heat, and thermal conductivity. Where possible, material properties extracted from experimentally obtained data on MQXF coil samples [11] were used rather than literature values; the interface contact resistance between solid materials and He II was also experimentally measured on a MQXF coil sample.
B. Mesh creation and refinement
The geometry was meshed using a Python API for the Meshing module of Salome 9.7, with specific refinement on the coil pack and thin layers such as insulation and helium passageway. The final mesh used for the numerical calculations is composed of 3.5 million cells.
C. Numerical solver description
The numerical solver used in this work was implemented in OpenFOAM v7, an open-source C++ toolbox for the development of computational models and libraries for solving continuum mechanics problems. A conjugate heat transfer solver was developed [12], combining a solver for heat conduction in composite solids and a solver for static He II (see Fig. 2).
Previously prohibitive computation time was drastically reduced by combining the calculation of the composite solid regions (cold mass and cold bore) into a single region, as such the complete geometry is composed of only two regions: a (composite) solid one, featuring many different zones each with its own material properties, and a pre-simulated He II region. The two regions interact by means of a buffer-layer boundary condition that implements experimentally measured [11] interface contact resistance between He I and solid materials, referred to as Kapitza resistance.

III. INPUT FOR SIMULATION
A. Energy deposition from collision debris
Debris from proton-proton collisions at the interaction points induce energy deposition in the superconducting magnets and respective cold masses, especially those in the insertion regions (IR) [13]. The power density deposited in the coils leads to an increase in temperature that is non-uniform throughout the cold mass structure.
The temperature increase due to debris-generated energy deposition needs to be evaluated to provide a more realistic operating temperature field for the magnets in the insertion regions. The energy deposition in the inner triplet magnets in the insertion regions (IR1 (ATLAS) and IR2 (CMS)) used as input for the present work was estimated by FLUKA for a baseline

for proton-proton collisions at 14 TeV for HL-LHC operation of the magnets that IR1, Q2A, Q2B, Q2C, and Q2D and vertical crossing in the cross-section at the cold mass; this is the only input that varies with each of the 12 modelled magnet cross-sections.
He II heat exchangers is set at a fixed temperature of 1.9 K (see Fig. 2). Finally, the power density map obtained with FLUKA (for a luminosity of $5.0 \times 10^{34} \text{ cm}^{-2} \text{ s}^{-1}$) and proton collisions at a center-of-mass energy of 14 TeV is applied to the entire cross-section of the MQXF coil and cold mass; this is the only input that varies with each of the 12 modelled magnet cross-sections.
IV. RESULTS
A. Temperature maps
Results consist of a temperature map for each selected magnet cross-section, an example of power density (a) and resulting temperature profile (b) is shown in Fig. 3 for the most exposed cross-section of Q2B at insertion region 1 (horizontal crossing). There is a localized hotspot in the cold bore, reaching 2.5 K, where the power density is highest.
Fig. 4 (a) shows the same temperature profile as Fig. 3, focused only on the coil itself. The coil shows a fairly homogeneous temperature distribution, with a maximum calculated temperature of 2.22 K on the outer layer, i.e. a 0.32 K gradient with respect to the cooling source in the saturated He II bath

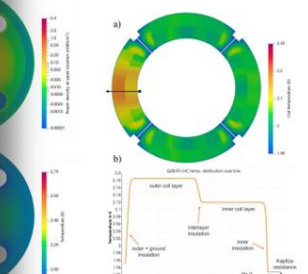


Fig. 3. (a) Temperature map for the MQXF coil and cold mass. (b) Temperature profile along the horizontal cold bore. The temperature profile shows a peak of 2.5 K in the cold bore, reaching 2.2 K on the outer layer, and a 0.32 K gradient with respect to the cooling source in the saturated He II bath.

the temperature distribution. The coil layer is insulated by the inner insulation, which is the most exposed cross-section of Q2B at insertion region 1 (horizontal crossing). There is a localized hotspot in the cold bore, reaching 2.5 K, where the power density is highest.
Fig. 4 (a) shows the same temperature profile as Fig. 3, focused only on the coil itself. The coil shows a fairly homogeneous temperature distribution, with a maximum calculated temperature of 2.22 K on the outer layer, i.e. a 0.32 K gradient with respect to the cooling source in the saturated He II bath

in the local temperature distribution. The coil layer is insulated by the inner insulation, which is the most exposed cross-section of Q2B at insertion region 1 (horizontal crossing). There is a localized hotspot in the cold bore, reaching 2.5 K, where the power density is highest.
Fig. 4 (a) shows the same temperature profile as Fig. 3, focused only on the coil itself. The coil shows a fairly homogeneous temperature distribution, with a maximum calculated temperature of 2.22 K on the outer layer, i.e. a 0.32 K gradient with respect to the cooling source in the saturated He II bath

Table 1. Temperature profiles in the MQXF power inputs, resulting from the power deposition at the most exposed cross-section of Q2B at insertion region 1 (horizontal crossing).

The coil pack			
Maximum temperature (K)	Maximum calculated temperature (K)	Average power density (W/cm ²)	Average temperature (K)
2.5	2.22	0.32	2.22
2.19	2.07	0.22	2.07
2.15	2.03	0.18	2.03
2.12	2.00	0.15	2.00
2.10	1.98	0.13	1.98
2.08	1.96	0.11	1.96
2.06	1.94	0.09	1.94
2.04	1.92	0.07	1.92
2.02	1.90	0.05	1.90
2.00	1.88	0.03	1.88
1.98	1.86	0.01	1.86
1.96	1.84	0.00	1.84
1.94	1.82	0.00	1.82
1.92	1.80	0.00	1.80
1.90	1.78	0.00	1.78
1.88	1.76	0.00	1.76
1.86	1.74	0.00	1.74
1.84	1.72	0.00	1.72
1.82	1.70	0.00	1.70
1.80	1.68	0.00	1.68
1.78	1.66	0.00	1.66
1.76	1.64	0.00	1.64
1.74	1.62	0.00	1.62
1.72	1.60	0.00	1.60
1.70	1.58	0.00	1.58
1.68	1.56	0.00	1.56
1.66	1.54	0.00	1.54
1.64	1.52	0.00	1.52
1.62	1.50	0.00	1.50
1.60	1.48	0.00	1.48
1.58	1.46	0.00	1.46
1.56	1.44	0.00	1.44
1.54	1.42	0.00	1.42
1.52	1.40	0.00	1.40
1.50	1.38	0.00	1.38
1.48	1.36	0.00	1.36
1.46	1.34	0.00	1.34
1.44	1.32	0.00	1.32
1.42	1.30	0.00	1.30
1.40	1.28	0.00	1.28
1.38	1.26	0.00	1.26
1.36	1.24	0.00	1.24
1.34	1.22	0.00	1.22
1.32	1.20	0.00	1.20
1.30	1.18	0.00	1.18
1.28	1.16	0.00	1.16
1.26	1.14	0.00	1.14
1.24	1.12	0.00	1.12
1.22	1.10	0.00	1.10
1.20	1.08	0.00	1.08
1.18	1.06	0.00	1.06
1.16	1.04	0.00	1.04
1.14	1.02	0.00	1.02
1.12	1.00	0.00	1.00
1.10	0.98	0.00	0.98
1.08	0.96	0.00	0.96
1.06	0.94	0.00	0.94
1.04	0.92	0.00	0.92
1.02	0.90	0.00	0.90
1.00	0.88	0.00	0.88
0.98	0.86	0.00	0.86
0.96	0.84	0.00	0.84
0.94	0.82	0.00	0.82
0.92	0.80	0.00	0.80
0.90	0.78	0.00	0.78
0.88	0.76	0.00	0.76
0.86	0.74	0.00	0.74
0.84	0.72	0.00	0.72
0.82	0.70	0.00	0.70
0.80	0.68	0.00	0.68
0.78	0.66	0.00	0.66
0.76	0.64	0.00	0.64
0.74	0.62	0.00	0.62
0.72	0.60	0.00	0.60
0.70	0.58	0.00	0.58
0.68	0.56	0.00	0.56
0.66	0.54	0.00	0.54
0.64	0.52	0.00	0.52
0.62	0.50	0.00	0.50
0.60	0.48	0.00	0.48
0.58	0.46	0.00	0.46
0.56	0.44	0.00	0.44
0.54	0.42	0.00	0.42
0.52	0.40	0.00	0.40
0.50	0.38	0.00	0.38
0.48	0.36	0.00	0.36
0.46	0.34	0.00	0.34
0.44	0.32	0.00	0.32
0.42	0.30	0.00	0.30
0.40	0.28	0.00	0.28
0.38	0.26	0.00	0.26
0.36	0.24	0.00	0.24
0.34	0.22	0.00	0.22
0.32	0.20	0.00	0.20
0.30	0.18	0.00	0.18
0.28	0.16	0.00	0.16
0.26	0.14	0.00	0.14
0.24	0.12	0.00	0.12
0.22	0.10	0.00	0.10
0.20	0.08	0.00	0.08
0.18	0.06	0.00	0.06
0.16	0.04	0.00	0.04
0.14	0.02	0.00	0.02
0.12	0.00	0.00	0.00

Fig. 4. (a) Temperature map for the MQXF coil and cold mass. (b) Temperature profile along the horizontal cold bore. The temperature profile shows a peak of 2.5 K in the cold bore, reaching 2.2 K on the outer layer, and a 0.32 K gradient with respect to the cooling source in the saturated He II bath.

the temperature distribution. The coil layer is insulated by the inner insulation, which is the most exposed cross-section of Q2B at insertion region 1 (horizontal crossing). There is a localized hotspot in the cold bore, reaching 2.5 K, where the power density is highest.
Fig. 4 (a) shows the same temperature profile as Fig. 3, focused only on the coil itself. The coil shows a fairly homogeneous temperature distribution, with a maximum calculated temperature of 2.22 K on the outer layer, i.e. a 0.32 K gradient with respect to the cooling source in the saturated He II bath

in the local temperature distribution. The coil layer is insulated by the inner insulation, which is the most exposed cross-section of Q2B at insertion region 1 (horizontal crossing). There is a localized hotspot in the cold bore, reaching 2.5 K, where the power density is highest.
Fig. 4 (a) shows the same temperature profile as Fig. 3, focused only on the coil itself. The coil shows a fairly homogeneous temperature distribution, with a maximum calculated temperature of 2.22 K on the outer layer, i.e. a 0.32 K gradient with respect to the cooling source in the saturated He II bath

Table 2. Temperature profiles in the MQXF power inputs, resulting from the power deposition at the most exposed cross-section of Q2B at insertion region 1 (horizontal crossing).

The coil pack			
Maximum temperature (K)	Maximum calculated temperature (K)	Average power density (W/cm ²)	Average temperature (K)
2.5	2.22	0.32	2.22
2.19	2.07	0.22	2.07
2.15	2.03	0.18	2.03
2.12	2.00	0.15	2.00
2.10	1.98	0.13	1.98
2.08	1.96	0.11	1.96
2.06	1.94	0.09	1.94
2.04	1.92	0.07	1.92
2.02	1.90	0.05	1.90
2.00	1.88	0.03	1.88
1.98	1.86	0.01	1.86
1.96	1.84	0.00	1.84
1.94	1.82	0.00	1.82
1.92	1.80	0.00	1.80
1.90	1.78	0.00	1.78
1.88	1.76	0.00	1.76
1.86	1.74	0.00	1.74
1.84	1.72	0.00	1.72
1.82	1.70	0.00	1.70
1.80	1.68	0.00	1.68
1.78	1.66	0.00	1.66
1.76	1.64	0.00	1.64
1.74	1.62	0.00	1.62
1.72	1.60	0.00	1.60
1.70	1.58	0.00	1.58
1.68	1.56	0.00	1.56
1.66	1.54	0.00	1.54
1.64	1.52	0.00	1.52
1.62	1.50	0.00	1.50
1.60	1.48	0.00	1.48
1.58	1.46	0.00	1.46
1.56	1.44	0.00	1.44
1.54	1.42	0.00	1.42
1.52	1.40	0.00	1.40
1.50	1.38	0.00	1.38
1.48	1.36	0.00	1.36
1.46	1.34	0.00	1.34
1.44	1.32	0.00	1.32
1.42	1.30	0.00	1.30
1.40	1.28	0.00	1.28
1.38	1.26	0.00	1.26
1.36	1.24	0.00	1.24
1.34	1.22	0.00	1.22
1.32	1.20	0.00	1.20
1.30	1.18	0.00	1.18
1.28	1.16	0.00	1.16
1.26	1.14	0.00	1.14
1.24	1.12	0.00	1.12
1.22	1.10	0.00	1.10
1.20	1.08	0.00	1.08
1.18	1.06	0.00	1.06
1.16	1.04	0.00	1.04
1.14	1.02	0.00	1.02
1.12	1.00	0.00	1.00
1.10	0.98	0.00	0.98
1.08	0.96	0.00	0.96
1.06	0.94	0.00	0.94
1.04	0.92	0.00	0.92
1.02	0.90	0.00	0.90
1.00	0.88	0.00	0.88
0.98	0.86	0.00	0.86
0.96	0.84	0.00	0.84
0.94	0.82	0.00	0.82
0.92	0.80	0.00	0.80
0.90	0.78	0.00	0.78
0.88	0.76	0.00	0.76
0.86	0.74	0.00	0.74
0.84	0.72	0.00	0.72
0.82	0.70	0.00	0.70
0.80	0.68	0.00	0.68
0.78	0.66	0.00	0.66
0.76	0.64	0.00	0.64
0.74	0.62	0.00	0.62
0.72	0.60	0.00	0.60
0.70	0.58	0.00	0.58
0.68	0.56	0.00	0.56
0.66	0.54	0.00	0.54
0.64	0.52	0.00	0.52
0.62	0.50	0.00	0.50
0.60	0.48	0.00	0.48
0.58	0.46	0.00	0.46
0.56	0.44	0.00	0.44
0.54	0.42	0.00	0.42
0.52	0.40	0.00	0.40
0.50	0.38	0.00	0.38
0.48	0.36	0.00	0.36
0.46	0.34	0.00	0.34
0.44	0.32	0.00	0.32
0.42	0.30	0.00	0.30

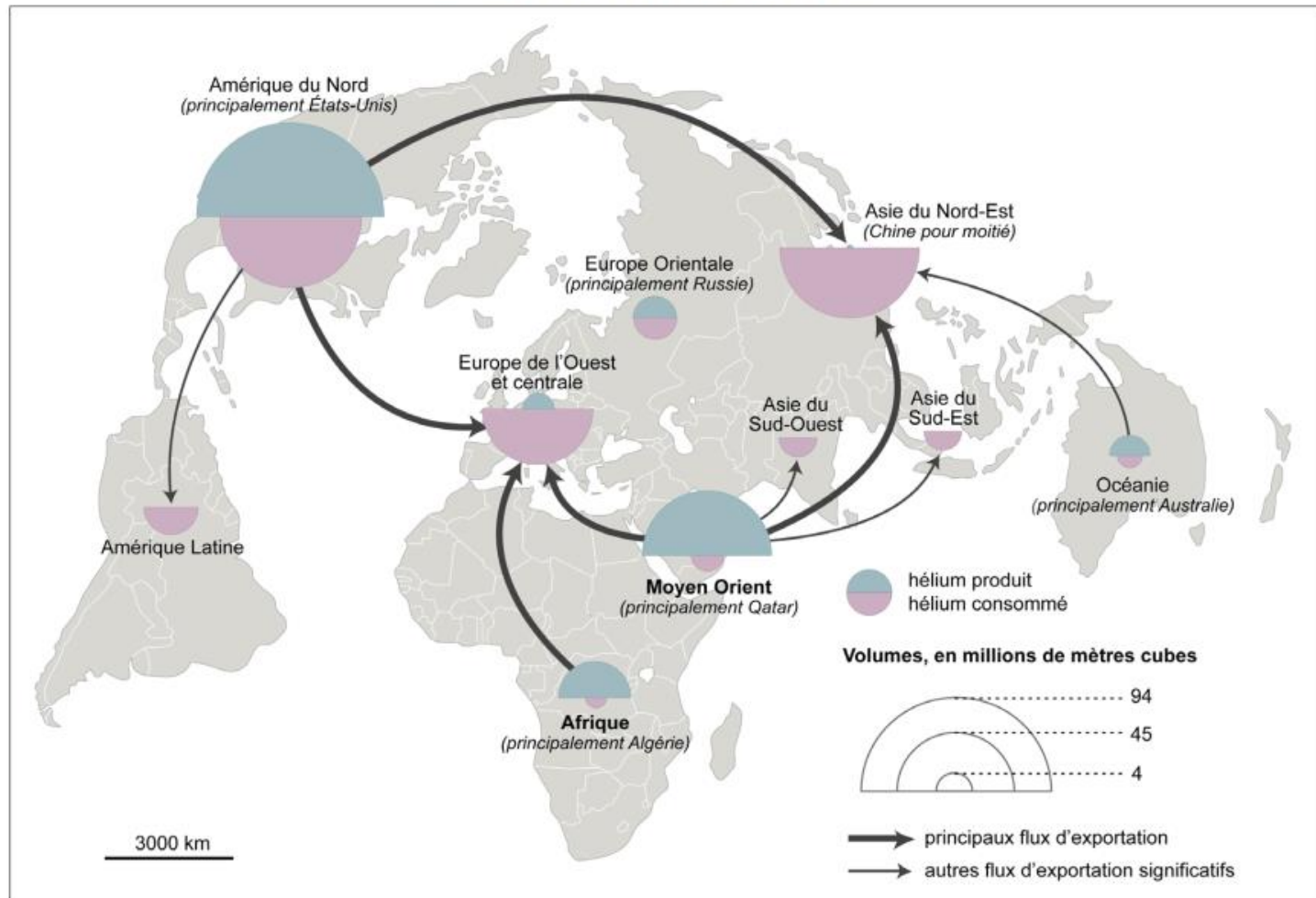
Helium availability and typical LHC reliance

(fully immersed magnets)

Next slides source: Frederic Ferrand (CERN Cryogenics)
see [7] for the full transcript

- Presentation based on available public information only
- Not an economist nor a seller, only interest is to supply necessary molecules for the laboratory in the coming years
- Helium market is currently (2022-data) evolving really fast and situation may be significantly different in a few months

Carte 1 : production, échanges et consommation d'hélium dans le monde en 2018



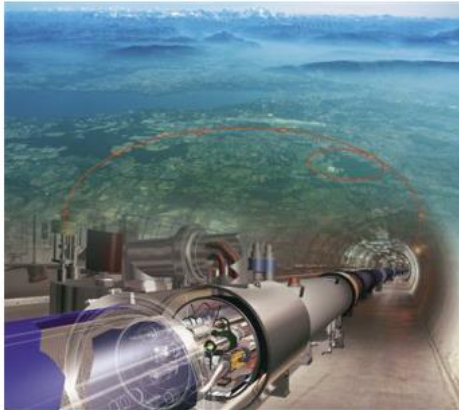
Source : Gubler et al. (2019).

Europe (and CERN) are outside supplier dependent

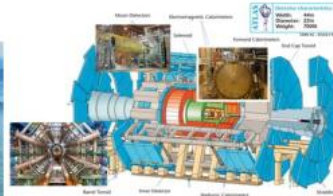
Ref: <https://www.ifri.org/fr/publications/briefings-de-lifri/helium-nouvelles-geographies-dune-ressource-critique>

Use of helium cryogenics at CERN

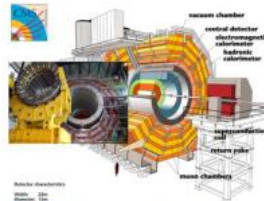
LHC & Experiments



LHC 36'000 tonnes of cold mass distributed over the 26.7 km underground accelerator



ATLAS 1'275 tonnes of cold mass



CMS 225 tonnes of cold mass

LHC accelerator cooling of the superconducting magnets at 1.9 K
ATLAS cooling at 4.5 K of the superconducting magnetic system
CMS cooling at 4.5 K of the superconducting solenoid

non-LHC & Test Facilities



SM18 test Facility



West Area test Facility



HIE Isolde Cryo Modules



SPS BA4 COLDEX



SPS BA6 Crab Cavities



Central Liquefier



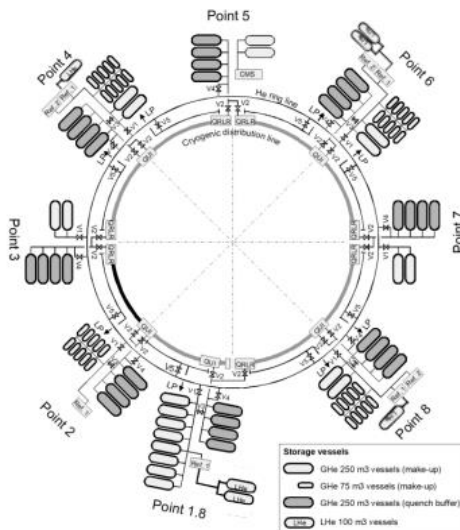
North Area

Test Benches for accelerator magnets, wires, RF cavities
non-LHC facilities and **fixed target physics experiments**
Central Helium liquefier and **Cryogenics laboratory**

Courtesy Frederic Ferrand

LHC infrastructure

Surface storage & distribution

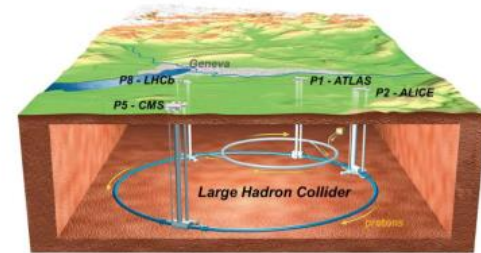


Gaseous helium storage 250m³



Liquid helium storage 250m³

Underground distribution & use



4.5K & 1.8K Cold Boxes

Distribution Valve Boxes

Distribution System



- Total inventory at CERN **175 tonnes** including **130 tonnes minimum for LHC**
- Distribution through the LHC Helium Ring Line, inter-sites High Pressure helium distribution line for non LHC and trailers

Courtesy Frederic Ferrand

Scope of supply for helium contracts 2022-2026

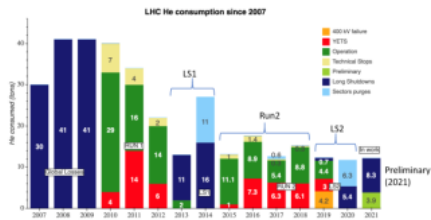
Liquid helium supply

200 tonnes

to compensate helium losses

Mainly for **testing and experiments**

For **LHC machine** constant effort to reduce losses showed results over the past 15 years



Helium quantities included:

- LHC needs for **Run 3** and refilling of the machine at the end of **Long Shutdown 3**
- Requirement for new **HL LHC cryogenic infrastructure** are also included

Helium management

140 tonnes

temporary sent out from CERN to contractual suppliers and returned on demand

This is a **necessary extension of CERN storage** capacity when LHC machine is partially or completely warm



During **Run year end closure** up to **20 tonnes** are sent out for about 2 months

During **Long Shutdowns** up to **80 tonnes** are sent out for about 18 months

Gaseous helium supply

6 tonnes

for LHC machine pressure tests

High Pressure helium trailers are used to pressurized sectors for safety pressure test



These deliveries are foreseen at the end of **Long Shutdown 3**

Courtesy Frederic Ferrand

Helium market long term evolution driven by US strategic decisions

Helium act 1925

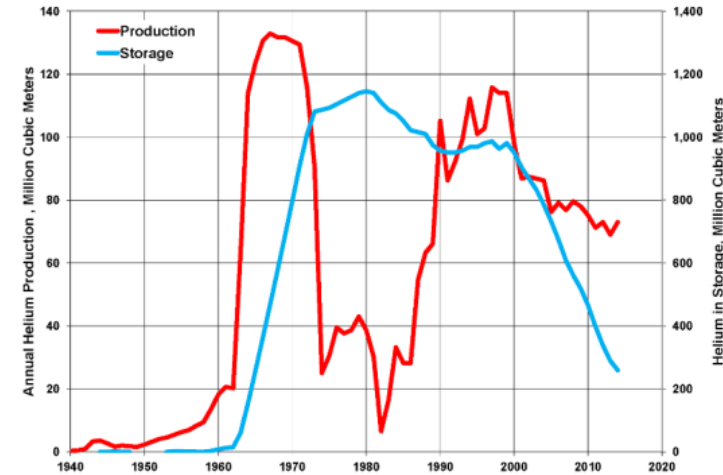
- Significant increase of the production in the 60's
- Cliffside infrastructure and underground storage of the federal strategic reserve
- Almost monopoly of the US on the worldwide helium market
- Rapid decrease of production in the 70's, reaching peak in 1980
- Managed by the state BLM with significant associated costs
- Confort zone, low prospecting and investment elsewhere

Helium privatization act in 1996

- Federal government expenses pay back by selling 1bcm till 2015
- Large industrial investment in Algeria 1997 and Qatar since 2008
- Production capacity developments in the private sector was too low

Stewardship Act of 2013

- Regulation of the of the market by selling of the strategic reserve through yearly auctions to the private sector
- Make the bridge with new international extraction capacity development
- Regulation of the US domestic market, but reduction of exports over the years



Wikipedia, based on US geological survey data

Good Read (in French): [IFRI Briefing](#)

Courtesy Frederic Ferrand

Known parameters affecting helium availability

- **Unbalanced supply and demand**, helium shortage 2006 & 2013
- **Geopolitical stability** in the country of extraction, Qatar 2017
- **Logistics complexity** blockage of Suez Canal in 2020
- **Maintenance shutdown or technical event** on LNG feed and helium liquefaction plants can impact market

Courtesy Frederic Ferrand

What's happening in 2022 ?

- **BLM closure in January**
 - Temporarily closed procedures for safe handling of chemical materials ([Gasworld](#))
 - Outsource of BLM operations to private contractor
- **Explosion at AMUR site in Russia production site in January**
 - Several events leading to stop of the commissioning ([Gasworld](#)) ;
 - Expecting ramp up of the production postponed
- **Commercial limitation with Russia due to conflict in Ukraine**
 - Impact on the AMUR project repair and recommissioning of the helium plant
 - Takeover of the engineering from European by a Chinese company
- **Planned maintenance during spring period**
- **Restart of industrial activities after Covid period**

Courtesy Frederic Ferrand

Consequences

Current situation

- Market shortage is affecting industrial and scientific customers
- Manufacturing industry contracts are impacted with volume limitations
- Large scientific instrument cannot do so & rely on established industrial partnership

Helium market still at risk in 2023 and for the coming years

- Uncertainty on the effective Russian production capacity and market access
- Algerian gas production transferred using pipeline instead of LNG
- No more back-up from the US federal authorities, Cliffside for sale ! ([C&en News](#))

Courtesy Frederic Ferrand

Perspective of new helium production capacities

- **LNG related**
 - Algeria debottlenecking of existing production sites
 - South Africa → 900Mm³ (lower estimate)
 - Qatar IV ?
- **Nitrogen-based helium production** ([Physicsworld article](#))
 - Canada (Gasworld [article 1](#) & [article 2](#)) → Announced production objectives 10% ww capacity by 2030
 - Tanzania ([The Citizen](#)) 54bcf of primary helium at Lake Rukwa → Production announced in 2025

Courtesy Frederic Ferrand

Food for thought of operating fully helium immersed accelerator magnets

Disclaimer: the LHC has been an immense success and functions marvelously. A 27 km long accelerator of which about 23 km at 1.9 K!

A cryogenic success, on both magnet cooling as well as the whole cryogenic infrastructure which functions with very high availability!

*However, there are a few points which are food for thought on whether we can do better for the next machine...
(whichever one that might be)*

Safety: avoiding trapped volumes

What happens if one neglects (or even forgets) radial passages!

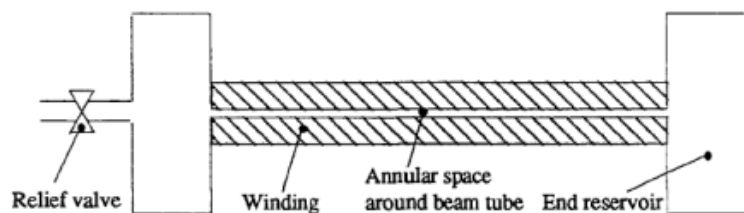
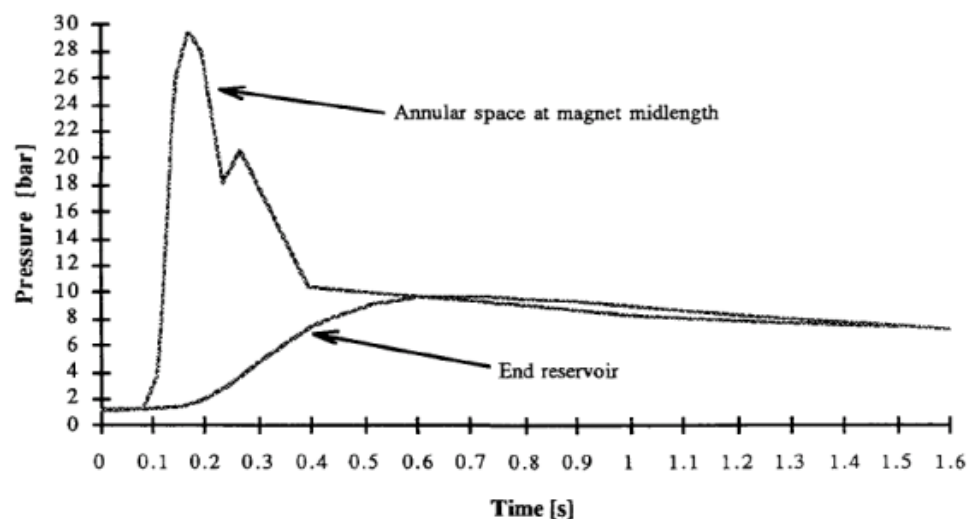
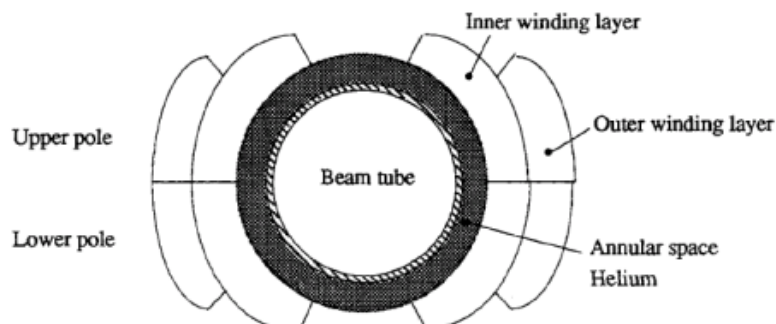


Figure 1.1 Dipole magnet



In a LHC-type cold-mass structure foreseen for a future 10 T coil, a low field (< 5 T) coil was placed, but to ease assembly a teflon sheet was mistakenly inserted between collar and yoke!

All radial escapes were closed, and even with the magnet energy of 5 T field, annular space pressures reached 30 bar.

A higher field coil of 10 T would have squeezed/distroyed the beam-pipe.

Safety: avoiding trapped volumes

- Since the experience with this very early stage LHC-cold mass test the explicit control of radial and longitudinal helium escape paths has become an integral part of the fully helium immersed magnet cold-mass designs and has never been an issue anymore

Safety: cold-mass pressure vessel

- A quench of a magnet-coil transfers about 25 % or more of the stored energy directly to the helium in which it is immersed
 - pressure built up would be of the order of > 200 bar if not managed by safety relief devices
 - The rate of pressure rise is coil-specific (porous or not p.e.) but initial adiabatic shock waves of several bar to about 10 bar cannot be avoided.
 - The pressure rating of the cold-mass due to the helium pressure rise phenomena may be higher than desired because of this (think of machine-detector-interface magnets p.e.)

Safety: containing helium spill consequences

The sheer amount of helium inside accelerator magnets has a heavy impact on personnel safety, especially in underground areas, and the infrastructure to deal with this:

- Helium release must be captured in dedicated cryogenic transfer lines
- Access restrictions for machine maintenance become dependent on the amount of helium in the cold-masses and their powering status
- Should accidents break the cold-mass to insulation vacuum helium will instead of being captured by the cryogenic transfer line spill into the ambient environment → Asphyxiation hazard

Inventory handling and supplier dependence

Some points to remember

Energy efficiency: Incorporate in the magnet design, whenever possible, features to intercept heat at as high T as possible!

Energy efficiency: If possible, use conductors that have a high T_c

Facilitating robust thermal design: Incorporate temperature margin to deal with heat extraction (no magnet operates at an ideal homogeneous temperature)

Inventory handling, supplier dependence, general & personnel safety: Aim for reduced helium content, preferably conduction cooled magnets

Selected References (1/3)

Books

“Experimental Techniques for Low-Temperature Measurements - Cryostat Design, Material Properties, and Superconductor Critical-Current Testing”, *Jack W. Ekin, Oxford University Press 2006, ISBN 0-19-857054-6 978-0-19-857054-7*

“Cryostat Design - Case Studies, Principles and Engineering”, *J.G. Weisend II, SPRINGER 2016, ISSN 0538-7051 ISSN 2199-3084 (electronic) International Cryogenics Monograph Series ISBN 978-3-319-31148-7 ISBN 978-3-319-31150-0 (eBook) DOI 10.1007/978-3-319-31150-0*

“Helium Cryogenics”, *Steven W. Van Sciver, SPRINGER, ISBN 978-1-4419-9978-8 e-ISBN 978-1-4419-9979-5 DOI 10.1007/978-1-4419-9979-5*

References (2/3)

- [1] COOLING STRINGS OF SUPERCONDUCTING DEVICES BELOW 2 K: THE HELIUM II BAYONET HEAT EXCHANGER, *Ph. Lebrun, L. Serio, L. Tavian and R. van Weelderen, LHC-project-report-144 / CEC-ICMC'97 - Portland - OR - USA July 28th - August 1st 1997*
- [2] SUPERFLUID HELIUM AS A TECHNICAL COOLANT, *Ph. Lebrun, LHC Project Report 125, Presented at 15th UIT National Heat Transfer Conference - Torino - Italy, June 19-20 1997*
- [3] Deduction of Steady-State Cable Quench Limits for Various Electrical Insulation Schemes with Application to LHC and HL-LHC Magnets, *Pier Paolo Granieri, Rob van Weelderen, CERN-ACC-2014-0035, 20/02/2014*
- [4] *Development and application of a generic CFD toolkit covering the heat flows in combined solid-liquid systems with emphasis on the thermal design of HiLumi superconducting magnets, Gennaro Bozza, Ziemowit M. Malecha, Rob Van Weelderen, Cryogenics-D-15-00175 (CHATS-2015 workshop)*

References (3/3)

- [5] An experimental and numerical framework to assess the temperature distribution in complex He II-cooled magnet geometries, *Kirtana Puthran, Patricia Borges de Sousa, Lise Murberga, Torsten Koettig, Rob van Weelderen, CHATS-AS 2023 Torino (to be published)*
- [6] Numerical assessment of the inhomogeneous temperature field and the quality of heat extraction from Nb₃Sn impregnated magnets for the High Luminosity upgrade of the LHC, *Patricia Borges de Sousa, Kirtana Puthran, Marta Sabaté-Gilarte, Francesco Cerutti, Susana Izquierdo Bermudez, Ezio Todesco, and Rob van Weelderen, ASC 2022 – Honolulu, (to be published)*
- [7] “Helium market considerations - Muon Magnets Working Group”, *Frederic Ferrand (CERN Cryogenics)*, <https://indico.cern.ch/event/1183565/>
- [8] “An Introduction to Cryogenics”, *Ph. Lebrun, CERN/AT 2007-1*, <https://cds.cern.ch/record/1012032?ln=fr>
- [9] “Heat Transfer and Cooling Techniques at Low Temperature”, *B. Baudouy, CAS - CERN Accelerator School: Superconductivity for Accelerators, pp.329-352*, <https://cds.cern.ch/record/1974061?ln=fr>